Charles University in Prague
Faculty of Mathematics and Physics

MASTER THESIS

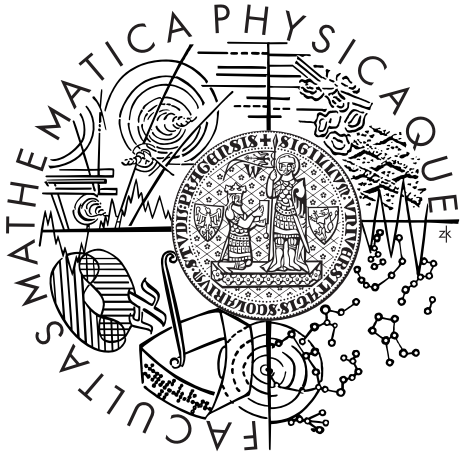

Stanislav Sláčík

Motion of a body in a fluid with pressure dependent viscosity

Mathematical Institute of Charles University

Supervisor of the master thesis:	Mgr. Vít Průša, PhD.
Study programme:	Physics
Specialization:	Mathematical and Computer Modelling in Physics and Engineering

Prague 2013

I would like to thank my supervisor, Mgr. Vít Průša, PhD., for his patient guidance and will to help.

My special thanks go to my consultant, RNDr. Jaroslav Hron, PhD., for lots of useful discussions concerning the finite element code, usage of the Sněhurka cluster and computational mathematics in general.

The access to computing and storage facilities owned by parties and projects contributing to the National Grid Infrastructure MetaCentrum, provided under the programme "Projects of Large Infrastructure for Research, Development, and Innovations" (LM2010005) is acknowledged.

The access to the CERIT-SC computing and storage facilities provided under the programme Center CERIT Scientific Cloud, part of the Operational Program Research and Development for Innovations, reg. no. CZ. 1.05/3.2.00/08.0144 is appreciated.

Last but not least, I would like to thank my parents for their generous support during the studies.

I declare that I carried out this master thesis independently, and only with the cited sources, literature and other professional sources.

I understand that my work relates to the rights and obligations under the Act No. 121/2000 Coll., the Copyright Act, as amended, in particular the fact that the Charles University in Prague has the right to conclude a license agreement on the use of this work as a school work pursuant to Section 60 paragraph 1 of the Copyright Act.

In ..... date ..... signature of the author

Název práce: Pohyb tělesa v tekutině s viskozitou závislou na tlaku

Autor: Stanislav Sláčík [s.slacik@seznam.cz]

Katedra: Matematický ústav UK

Vedoucí diplomové práce: Mgr. Vít Průša, PhD. [prusv@karlin.mff.cuni.cz]

Abstrakt: Mnoho technologicky důležitých nestlačitelných tekutin vykazuje silnou závislost viskozity na tlaku; k měření je často užíván viskometr s padajícím válcem, přičemž viskozita je určena nepřímo z doby pádu závaží o danou vzdálenost. Užívaný vztah mezi rychlostí pádu válce a viskozitou kapaliny je však odvozen za předpokladu konstantní vazkosti. Cílem této práce je provést numerickou simulaci viskometrického experimentu s předpokladem explicitní závislosti viskozity na tlaku a realistickými materiálovými parametry a kvantifikovat odchylky v pohybu tělesa oproti běžně užívanému Navierově-Stokesově modelu. Navržená výpočetní metoda pro řešení problému s nelineárním konstitutivním vztahem a volným pohybem tělesa (tj. v časově závislé oblasti) je ověřena na jednoduchých problémech s analytickým řešením. Odvozený semianalytický vztah pro Navierovu-Stokesovu tekutinu je porovnáván s výsledky numerických simulací; pozornost je věnována rovněž vlivu geometrie viskometru na platnost předpokladů v teoretickém odvození.

Klíčová slova: Pádový viskometr, viskozita závislá na tlaku, chyba měření.

Title: Motion of a body in a fluid with pressure dependent viscosity

Author: Stanislav Sláčík

Department: Mathematical Institute of Charles University

Supervisor: Mgr. Vít Průša, PhD. [prusv@karlin.mff.cuni.cz]

Abstract: A lot of technologically relevant incompressible fluids exhibit a substantial variaton of viscosity with the pressure; a falling cylinder viscometer is frequently used for the measurements, determining the viscosity indirectly from the time it takes the sinker to fall a given distance. The relation between the sinker fall velocity and the fluid viscosity is, however, derived under the constant viscosity assumption. The objective of the present thesis is to perform a numerical simulation of the viscometric experiment, assuming an explicit form of the pressure-viscosity dependence and realistic parameter values and to quantitatively assess the difference in body motion to the Navier-Stokes model. The computational method proposed, handling both the nonlinear constitutive relation and the body motion, was tested on simple problems with analytical solutions. The semianalytical relation for the Navier-Stokes model, also re-derived here, is compared to the computational results. The validity of the assumptions used in the theoretical derivation, based on the results of the numerical simulation, is discussed regarding the geometry of the viscometer.

Keywords: Falling cylinder viscometer, pressure-dependent viscosity, experimental error.

Contents

Introduction

Accurate viscosity measurement under high pressure is a vital issue in industry and applied physics. Several methods are available; the *falling cylinder* method, dating back to the pioneering work of P. W. Bridgman [1], is among the most popular. The experimental methodology, based on a relation between the time of fall and the viscosity, intrinsically assumes a perfectly constant viscosity of the fluid, even though the viscosity is observed to increase rapidly with increasing pressure. Possible inconsistency in such measurements was discussed by Průša, Srinivasan and Rajagopal [2] using perturbation analysis. They conclude that despite the effect is small, it is measurable with contemporary equipment.

The aim of this work is to extend the results of [2] and perform numerical simulation of the experiment with a falling cylinder viscometer in an incompressible fluid with pressure-dependent viscosity with relation

$$\mu = \mu_0 \exp[\beta(p - p_0)].$$

From the computational point of view, both the motion of a body in a fluid and the flow of a piezoviscous fluid are very involved tasks themselves. The complexity of the problem is further enhanced by need to use realistic parameter values as occuring in the experiments.

The present text is organized as follows: The problem of the body motion in a viscous fluid is formulated in the first chapter and relevant constitutive assumptions are proposed. Unlike many papers concerning the mathematical theory of incompressible flows with pressure-dependent viscosity published recently, no dependence of the fluid viscosity on shear rate will be considered.

The second chapter is devoted to a brief summary concerning a falling cylinder viscometer. Certain simplifying assumptions are made and a theoretical formula for the settling velocity of a cylinder in a Newtonian fluid is derived.

Third chapter provides a conceptual description of the academic finite element solver used in the simulations.

The remaining chapters describe consecutive steps of the devision of the numerical method; the rate of convergence of the finite elements is demonstrated on simple flows of liquids with pressure-depenedent viscosity. Then the problem of a falling cylinder is transformed to a two-dimensional analogue and auxiliary results for the Newtonian fluid are used in the the problem with cylindrical symmetry.

A numerical estimate of the end effects for a cylinder with flat ends is given. The results for the fall of a body in a fluid with pressure-dependent viscosity are given in the end of Chapter 6. Liability of the results in terms of computational accuracy and realistic nature of the parameter values is discussed as well.

1. Motion of a body in a viscous fluid

1.1 Governing equations

Consider a rigid body $\mathcal{B}$, surrounded by a viscous fluid in a domain $\hat{\Omega} \subset \mathbb{R}^3$. The motion is described by the centre-of-mass position vector $\mathbf{r}_b(t)$ and the rotational matrix $\mathbb{Q}(t) \in SO(3)$ corresponding to the rotation of the body around its centre of mass. The translational velocity $\mathbf{v}_b$ is defined as the time derivative of the position

$$\mathbf{v}_b = \frac{\mathrm{d}\mathbf{r}_b}{\mathrm{d}t}; \tag{1.1}$$

the angular velocity $\boldsymbol{\omega}$ is defined as a vector satisfying

$$\boldsymbol{\omega} \times \mathbf{a} = \frac{\mathrm{d}\mathbb{Q}}{\mathrm{d}t}\mathbb{Q}^T\mathbf{a} \quad \forall \mathbf{a} \in \mathbb{R}^3. \tag{1.2}$$

The body translational motion is governed by the equation of motion (Newton's second law)

$$m\frac{\mathrm{d}\mathbf{v}_b}{\mathrm{d}t} = \mathbf{F}, \tag{1.3}$$

where m is the mass of the body and $\mathbf{F}$ total force acting on the body. The rate of change of the angular velocity is related to the total torque $\mathbf{M}$ exerted as follows:

$$\mathbb{J}\frac{\mathrm{d}\boldsymbol{\omega}}{\mathrm{d}t} = \mathbf{M}, \tag{1.4}$$

$\mathbb{J}$ being the moment of inertia tensor.

The fluid around the body satisfies conservation of mass and momentum, expressed in the Eulerian form as

$$\frac{\partial \rho_f}{\partial t} + \nabla \cdot (\rho_f \mathbf{v}) = 0, \tag{1.5}$$

$$\frac{\partial (\rho_f \mathbf{v})}{\partial t} + \nabla \cdot (\rho_f \mathbf{v} \otimes \mathbf{v}) = \nabla \cdot \mathbb{T} + \rho_f \mathbf{b} \qquad \text{in } \hat{\Omega} \setminus \mathcal{B}(t), \tag{1.6}$$

where $\mathbf{b}$ is the specific body force (e. g. graviational,) ρ_f is the fluid density, $\mathbf{v}$ the fluid velocity, $\mathbb{T}$ the Cauchy stress tensor. A viscous fluid tends to adhere on rigid walls; therefore we require

$$\mathbf{v}(\mathbf{x}, t) = \mathbf{v}_b(t) + \boldsymbol{\omega}(t) \times (\mathbf{x} - \mathbf{r}_b), \quad \mathbf{x} \in \partial\mathcal{B}$$

as a boundary condition. In the absence of internal couples we may state the conservation of angular momentum in the fluid as

$$\mathbb{T} = \mathbb{T}^T.$$

The total force acting on the body can be written in two components

$$\mathbf{F} = \int_{\mathcal{B}} \rho_b \mathbf{b} \, \mathrm{d}x + \mathbf{F}_f,$$

m denoting the mass of the body $\mathcal{B}$, $\mathbf{b}$ the density of volume forces; $\mathbf{F}_f$ is the force of reaction of the fluid given by surface integral over the surface of the body

$$\mathbf{F}_f = \oint_{\partial\mathcal{B}} \mathbb{T} \cdot \mathbf{n} \, \mathrm{d}S, \tag{1.7}$$

where $\mathbb{T}$ is the Cauchy stress tensor and $\mathbf{n}$ outwards-pointing normal vector to the body surface. Similarly, the torque is given by

$$\mathbf{M} = \oint_{\partial\mathcal{B}} (\mathbf{x} - \mathbf{r}_b) \times \mathbb{T}\mathbf{n} \, \mathrm{d}S + \int_{\mathcal{B}} \rho_f (\mathbf{x} - \mathbf{r}_b) \times \mathbf{b} \, \mathrm{d}x; \tag{1.8}$$

for conservative forces the second term vanishes.

1.2 Constitutive laws

Apart from the initial and boundary conditons, additional information must be supplied in order to close the system (1.1)–(1.8). In particular, the fluid momentum equation (1.6) lacks a relation between the fluid velocity and the fluid stress tensor. Such a relation is called a *constitutive relation*. We will present some simplifying assumptions first.

1.2.1 Basic assumptions

An *incompressible fluid* satisfies

$$\nabla \cdot \mathbf{v} = 0; \tag{1.9}$$

this constraint implies that the density of the material point[1] remains constant:

$$\frac{\mathrm{d}\rho_f}{\mathrm{d}t} = 0.$$

Furthermore, we will assume $\rho_f = \text{const.}$ in the whole domain, treating *homogeneous fluids* only. The condition (1.9) is then met identically. With the help of continuity equation (1.5) and the constant density assumption, the fluid momentum equation (1.6) can be rewritten as

$$\rho_f \left[\frac{\partial \mathbf{v}}{\partial t} + (\mathbf{v} \cdot \nabla)\mathbf{v} \right] = \nabla \cdot \mathbb{T} + \rho_f \mathbf{b}. \tag{1.10}$$

In fact, real liquids are not perfectly incompressible, but the effect is small enough to neglect it even at high pressures.

A constant temperature will be assumed in all computations as well.

1.2.2 Particular forms of the Cauchy stress tensor

A constitutive relation to be used is

$$\mathbb{T} = -p\mathbb{I} + 2\mu(p)\mathbb{D}, \tag{1.11}$$

[1] see e. g. [3], page 60.

$\mathbb{I}$ being the identity tensor and $\mathbb{D}$ the symmetric velocity gradient

$$\mathbb{D} = \frac{1}{2}\left[\nabla \mathbf{v} + (\nabla \mathbf{v})^T\right]. \tag{1.12}$$

Using (1.9), we see that

$$\text{Tr } \mathbb{D} = \nabla \cdot v = 0;$$

the scalar p – the pressure – is therefore the mean normal stress

$$p = -\frac{1}{3}\text{Tr } \mathbb{T}$$

and it can be viewed as a Lagrange multiplier for the incompressibility constraint (1.9).

The dependence of the shear viscosity μ on the pressure will be modelled by the Barus equation [5]

$$\mu(p) = \mu_0 \exp[\beta(p - p_0)], \tag{1.13}$$

with the *pressure-viscosity coefficient* β being a positive constant. This model is justified by numerous experimental studies (see e. g. [6], [7], [9], [1]), even though it has certain limitations [1], [10]. Since the parameter β is very small for real liquids, it is often convenient to work with the linearised form

$$\mu(p) = \mu_0[1 + \beta(p - p_0)]. \tag{1.14}$$

Note that the dependence of the viscosity on the pressure renders these models implicit. Setting $\beta = 0$ in (1.13) we recover the well known Navier-Stokes (Newtonian) model

$$\mathbb{T} = -p\mathbb{I} + 2\mu_0\mathbb{D} \tag{1.15}$$

with μ_0 constant.

Substituting (1.15) into the fluid momentum balance (1.6) gives rise to *incompressible Navier-Stokes* equations

$$\nabla \cdot \mathbf{v} = 0, \tag{1.16a}$$

$$\rho_f \frac{\partial v}{\partial t} + \rho_f(\mathbf{v} \cdot \nabla)\mathbf{v} = -\nabla p + \mu_0 \Delta \mathbf{v}. \tag{1.16b}$$

1.3 Weak formulation of the flow equations

From [(1.9),(1.10),(1.11)] we will now derive a formulation suitable for use in finite element solvers – a *weak formulation*. First, we will assume that the Dirichlet boundary data $[\Gamma_D, \mathbf{v}_D; |\Gamma_D| > 0]$ is provided. Then, choosing an arbitrary smooth function

$$\boldsymbol{\varphi} \in \mathcal{X} = \{\boldsymbol{\varphi} \in \boldsymbol{C}^\infty(\Omega), \boldsymbol{\varphi} = 0 \text{ on } \Gamma_D\},$$

multiplying both sides of (1.10) with $\boldsymbol{\varphi}$ and integrating over Ω we obtain

$$\int_\Omega \rho_f \frac{\partial \mathbf{v}}{\partial t} \cdot \boldsymbol{\varphi} + [(\mathbf{v} \cdot \nabla)\mathbf{v}] \cdot \boldsymbol{\varphi} \, \mathrm{d}x = \int_\Omega (\nabla \cdot \mathbb{T}) \cdot \boldsymbol{\varphi} + \rho_f \mathbf{b} \cdot \boldsymbol{\varphi} \, \mathrm{d}x.$$

Now we may use integration by parts to eliminate the derivative of $\mathbb{T}$. Taking into account the boundary data and the stress symmetry (i. e. the balance of angular momentum,) the relation is rewritten as

$$\int_\Omega \rho_f \frac{\partial \mathbf{v}}{\partial t} \cdot \boldsymbol{\varphi} + [(\mathbf{v} \cdot \nabla)\mathbf{v}] \cdot \boldsymbol{\varphi} + \mathbb{T} : \nabla \boldsymbol{\varphi} \, \mathrm{d}x = \int_\Omega \rho_f \mathbf{b} \cdot \boldsymbol{\varphi} \, \mathrm{d}x + \int_{\Gamma_N} \mathbb{T}\mathbf{n} \cdot \boldsymbol{\varphi} \, \mathrm{d}S. \quad (1.17)$$

Since $\boldsymbol{\varphi}$ was chosen arbitrarily, (1.17) should hold for all $\boldsymbol{\varphi} \in \mathcal{X}$. Following the same procedure, we define the space $\mathcal{Y} = \{\psi \in C^\infty(\Omega)\}$ and state the continuity equation as

$$\int_\Omega (\nabla \cdot \mathbf{v}) \psi \, \mathrm{d}x = 0 \quad \forall \psi \in \mathcal{Y}. \quad (1.18)$$

Taking the closure of $\mathcal{X}, \mathcal{Y}$ in appropriate norms, one is able to generalise the notion of a solution to the equations [(1.9),(1.10),(1.11)].

For the particular case of fixed domain $\tilde{\Omega}$, the solution $[\mathbf{v}, p]$ of the weak problem is sought in spaces[2]

$$\mathbf{V} = \left\{ \mathbf{u} \in L^2(0,T;\mathbf{X}) \cup L^\infty(0,T;\mathbf{L}^2(\tilde{\Omega})), \frac{\partial \mathbf{u}}{\partial t} \in \mathbf{L}^1(0,T;\mathbf{X}') \right\}$$
$$U = L^2(0,T;Y)$$

with

$$\mathbf{X} = \{\boldsymbol{\varphi} \in \mathbf{W}^{1,2}(\tilde{\Omega}), \gamma_D(\boldsymbol{\varphi}) = 0 \text{ in } \mathbf{W}^{\frac{1}{2},2}(\Gamma_D)\}$$
$$Y = L^2(\tilde{\Omega})$$

as the spaces of test functions.

The *weak formulation* of the flow equations in fixed domain $\tilde{\Omega}$ is stated as follows: Find $\mathbf{v}(\mathbf{x},t) \in \mathbf{V}, p \in U$ such that

$$\mathbf{v}|_{\Gamma_D} = \mathbf{v}_D \quad (1.19a)$$
$$\mathbf{v}(x,0) = \mathbf{v}_0(x) \quad (1.19b)$$
$$\int_{\tilde{\Omega}} \rho_f \frac{\partial \mathbf{v}}{\partial t} \cdot \mathbf{w} + \rho_f (\mathbf{v} \cdot \nabla \mathbf{v}) \cdot \mathbf{w} - p(\nabla \cdot \mathbf{w}) + 2\mu(p)\mathbb{D}(\mathbf{v}) : \mathbb{D}(\mathbf{w}) \, \mathrm{d}x = \int_\Omega \rho_f \mathbf{b} \cdot \mathbf{w} \, \mathrm{d}x + \int_{\Gamma_N} \mathbb{T}\mathbf{n} \cdot \mathbf{w} \, \mathrm{d}S \quad \forall \mathbf{w} \in \mathbf{X} \quad (1.19c)$$
$$\int_{\tilde{\Omega}} q(\nabla \cdot \mathbf{v}) \, \mathrm{d}x = 0 \quad \forall q \in Y \quad (1.19d)$$

Nevertheless, we are not essentially interested in exact identity of the spaces $\mathbf{X}$, Y as the aim of the present work is to look into numerical solutions; this will be done by means of the *Galerkin approximation*. We will choose suitable

[2] An usal approach in the mathematical theory of the incompressible flow is to seek the solution in spaces of functions with vanishing divergence, adding a condition $\nabla \cdot \boldsymbol{\varphi} = 0$ in the definition of the space $\mathcal{X}$. Such a formulation is not, however, siutable to use in numerical calculations, since it is very difficult to construct finite-dimensional spaces of divergence-free functions with sufficient approximational properties.

finite-dimensional subspaces $\mathbf{X}_h \subset \mathbf{X}$, $Y_h \subset Y$ and seek $\mathbf{v}_h$, p_h such that (1.19c, 1.19d) hold for all $\mathbf{w}_h \in \mathbf{X}_h$, $q_h \in Y_h$. Actually, this is the framework of the finite element (FEM) method; its application to flows of incompressible fluids with pressure-dependent viscosity is a relatively recent topic [11],[12]. These works, however, consider the viscosity in the form

$$\mu(p, |\mathbb{D}|^2) = \mu_0[A + (1 + \exp(\beta p))^{-q} + |\mathbb{D}|^2]^{\frac{r-2}{2}},$$

which is substantially different from (1.13). Analysis of flows with viscosity depending solely on the pressure is a rather cumbersome issue; see [13], [14].

2. Falling cylinder viscometer

2.1 Overview

A falling body setup is a suitable choice for viscosity measurement of liquids under high pressures [15]. Neglecting the inertial effects of the fluid (e. g. at small velocities of the body,) the body is exposed to three kinds of force – the gravitational force, the buoyancy due to the Archimedes law and the viscous drag, dependent on both the viscosity and fluid velocity, Released from rest, the body speeds up until a balance between the three forces is reached. If the fluid is Newtonian, the force equilibrium is stable, meaning that a constant *terminal velocity* of the sinker is attained. Once the sinker is in the steady fall regime, one is able to measure the time it takes the sinker to fall a certain distance; the time then can be related to the fluid viscosity.

A measurement with falling cylinder viscometer conceptually resembles the Stokes method, based on a solution for a slow motion of a sphere in Euclidean space $\mathbb{R}^3$. Both the metods rely on the *creeping flow* approximation, valid at low values of Reynolds number. While the Stokes method achieves low Re values of the flow through use of spheres with small diametres, in the case of a falling cylinder viscometer (FCV) the sinker has a radius very close to the inner radius of the container, creating a narrow gap between the sinker and the tube. This approach helps to reduce statistical error of the fall time, as the terminal velocity is small. Moreover, such a geometry requires realtively small quantity of the experimental sample as opposed to the Stokes method [16].

2.2 Problem geometry

A falling cylinder viscometer consists of a cylindrical tube of internal radius R_2 and height H, filled by fluid under examination. A sinker, being a homogeneous circular cylinder with radius R_1 and height h, is placed coaxially[1] within the tube, let to fall freely in the fluid. Figure 2.1 describes the problem dimensions; we see that the problem is symmetric about the z axis, suited to make use of cylindric coordinates.

The sinker is released from rest. The gravitational field is assumed homogeneous

$$\mathbf{b} = -g\mathbf{e}_z.$$

Since the body forces are conservative ($\nabla \times \mathbf{b} \equiv \mathbf{0}$), no torque on the body is exerted. Consequently, the sinker does not rotate:

$$\boldsymbol{\omega} \equiv \mathbf{0}.$$

[1]The eccentricity of the sinker is carefully considered in the experiments [17] as the wrong position of the sinker may vitiate the measurement. In order to enhance self-centering properties of the sinker is the front face of the sinker of a hemispherical shape [1] and the centre of mass is lowered; see e.g. [18] or [6].

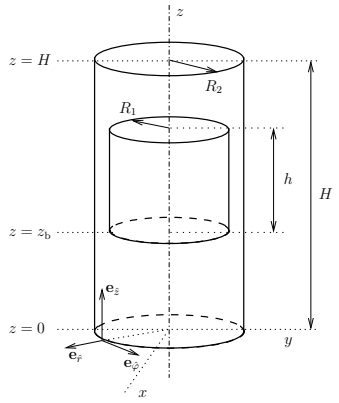

Figure 2.1: Dimensions of the falling cylinder viscometer. Courtesy of Průša *et al.* [2]

2.3 Terminal velocity for the FCV

Let us now determine the falue of settling velocity for the falling cylinder viscometer in a Newtonian fluid, neglecting the inertia effects. First, we will specify the flow around the body at a given velocity v_b. Recall that the governing equations for the Newtonian fluid take the form

$$\nabla \cdot \mathbf{v} = 0, \tag{1.16a}$$

$$\rho_f \frac{\partial \mathbf{v}}{\partial t} + \rho_f (\mathbf{v} \cdot \nabla)\mathbf{v} = -\nabla p + \mu_0 \Delta \mathbf{v}. \tag{1.16b}$$

The boundary conditions are assumed

$$\mathbf{v}(\partial\Omega) = \mathbf{0},$$

$$\mathbf{v}(\partial\mathcal{B}) = \mathbf{v}_b,$$

with $\partial\Omega$ denoting the container walls and $\partial\mathcal{B}$ the sinker surface. As a consequence of incompressibility the *volumetric flow* is conserved throughout the tube. In particular, we require

$$v_b^z S_s = \int_{\Sigma_T - \Sigma_S} \mathbf{v} \cdot \mathbf{e}_z \, \mathrm{d}S, \tag{2.1}$$

where S_s is the cross-sectional area of the cylinder, $\Sigma_T - \Sigma_S$ is the cross section of the annular gap between the tube and the sinker.

We will now proceed to derive the relation between velocity of the sinker and the force exerted by fluid. The problem geometry permits to assume an unidirectional flow in the gap between the sinker and the container wall:

$$\mathbf{v} = v^z(r)\mathbf{e}_z.$$

Moreover, we neglect all end effects; we consider the annular region between the walls only, merely investigating the flow between two infinite cylindrical walls. Viewed from the "laboratory" frame of reference, the outer wall is fixed, while the inner slides down the z coordinate with velocity $\mathbf{v}_b = v^*\mathbf{e_z}$. Then (1.16) simplifies a to scalar equation

$$\mu \left(\frac{\partial^2 v^z}{\partial r^2} + \frac{1}{r}\frac{\partial v^z}{\partial r} \right) = \frac{\partial p}{\partial z} + \rho_f g \tag{2.2}$$

in polar coordinates. The ansatz $\mathbf{v} = v^z(r)\mathbf{e_z}$ fulfills the continuity equation $\nabla\cdot\mathbf{v} = 0$. While the left-hand side of the equation (2.2) is a function of r entirely, the only way to satisfy (1.16) with the chosen ansatz is to assume $p = p(z)$. Hence, both sides of the equation (2.2) must be equal to a constant U. The flow is investigated in the annular region only, where is $r > 0$; thus

$$\frac{\partial p}{\partial z} - \rho_f g = U,$$

$$\mu\left(r\frac{\mathrm{d}^2 v^z}{\mathrm{d}r^2} + \frac{\mathrm{d}v^z}{\mathrm{d}r}\right) = Ur.$$

Let us now derive the expression for the fluid velocity in the gap. Rearranging using Leibniz rule,

$$\frac{\mathrm{d}}{\mathrm{d}r}\left(r\frac{\mathrm{d}v^z}{\mathrm{d}r}\right) = \frac{1}{\mu}Ur,$$

both sides of the equation can now be integrated to yield

$$r\frac{\mathrm{d}v^z}{\mathrm{d}r} = \frac{1}{2\mu}Ur^2 + A.$$

After dividing by r we are able to perform another integration, arriving at

$$v^z(r) = \frac{1}{4\mu}Ur^2 + A\ln r + B.$$

Using no-slip condition at $r = R_2$, we rewrite the velocity as

$$v^z(r) = \frac{1}{4\mu}U(r^2 - R^2) + A\ln\frac{r}{R_2}$$

and then employ the boundary condition at $r = R_1$ to relate A to U:

$$v^* = \frac{1}{4\mu}U(R_1^2 - R_2^2) + A\ln\frac{R_1}{R_2},$$

$$A = \frac{1}{\ln\frac{R_1}{R_2}}\left[v^* - \frac{1}{4\mu}U(R_1^2 - R_2^2)\right].$$

The value of U is found through the flux condition (2.1):

$$2\pi\int_{R_1}^{R_2} rv^z(r)\ \mathrm{d}r = -v^*\pi R_1^2.$$

Evaluating the integral on the left hand side

$$\left[\frac{U}{4\mu}\left(\frac{r^4}{4} - \frac{R_2^2 r^2}{2}\right) + \frac{A}{2}r^2\left(\ln\frac{r}{R_2} - \frac{1}{2}\right)\right]_{R_1}^{R_2} = -v^*\frac{R_1^2}{2},$$

$$\frac{U}{4\mu}\left[\frac{R_2^4 - R_1^4}{4} - \frac{R_2^2}{2}(R_2^2 - R_1^2)\right] + \frac{A}{2}\left[-\frac{1}{2}R_2^2 - R_1^2\left(\ln\frac{R_1}{R_2} - \frac{1}{2}\right)\right] = -v^*\frac{R_1^2}{2},$$

$$-\frac{U}{16\mu}\left(R_1^2 - R_2^2\right)^2 + \frac{A}{4}\left(R_1^2 - R_2^2 - 2R_1^2\ln\frac{R_1}{R_2}\right) = -v^*\frac{R_1^2}{2},$$

and substituting for A,

$$-\frac{U}{16\mu}\left(R_1^2-R_2^2\right)^2+\frac{v^*-\frac{U}{4\mu}(R_1^2-R_2^2)}{4\ln\frac{R_1}{R_2}}\left(R_1^2-R_2^2-2R_1^2\ln\frac{R_1}{R_2}\right)=-v^*\frac{R_1^2}{2},$$

we rearrange the equation as follows:

$$-\frac{U}{16\mu}(R_1^2-R_2^2)\left[(R_1^2-R_2^2)+\frac{R_1^2-R_2^2-2R_1^2\ln\frac{R_1}{R_2}}{\ln\frac{R_1}{R_2}}\right]$$
$$=-v^*\left[\frac{R_1^2}{2}+\frac{\left(R_1^2-R_2^2-2R_1^2\ln\frac{R_1}{R_2}\right)}{4\ln\frac{R_1}{R_2}}\right]$$

$$-\frac{U}{4}(R_1^2-R_2^2)\left[(R_1^2-R_2^2)\ln\frac{R_1}{R_2}+R_1^2-R_2^2-2R_1^2\ln\frac{R_1}{R_2}\right]$$
$$=-\mu v^*\left[2R_1^2\ln\frac{R_1}{R_2}+\left(R_1^2-R_2^2-2R_1^2\ln\frac{R_1}{R_2}\right)\right]$$

$$-\frac{U}{4}(R_1^2-R_2^2)\left[R_1^2-R_2^2-(R_1^2+R_2^2)\ln\frac{R_1}{R_2}\right]=-\mu v^*\left(R_1^2-R_2^2\right)$$

$$U=\frac{4\mu v^*}{R_1^2-R_2^2-(R_1^2+R_2^2)\ln\frac{R_1}{R_2}}. \tag{2.3}$$

Total reactional force of the fluid on the cylinder

$$\mathbf{F}_r=\oint_{\partial\mathcal{B}}\mathbb{T}\mathbf{n}\,\mathrm{d}S=\mathbf{F}_{buoy}+\mathbf{F}_{drag}$$

can be written in two components – the buoyancy

$$\mathbf{F}_{buoy}=\int_{\text{bases}}\mathbb{T}\mathbf{n}\,\mathrm{d}S,$$

and the viscous drag[2]

$$\mathbf{F}_{drag}=\int_{\text{lateral area}}\mathbb{T}\mathbf{n}\,\mathrm{d}S.$$

Under the assumptions made above, these formulae simplify to

$$\mathbf{F}_{buoy}=\pi R_1^2 p(z)|_{z=z_b}-p(z)|_{z=z-b+h}\,\mathrm{d}z\,\mathbf{e}_z=\pi R_1^2 h(\rho_f g-U)\mathbf{e}_z\equiv F_b\mathbf{e}_z, \tag{2.4}$$

$$\mathbf{F}_{drag}=2\pi R_1 h\,\mu\frac{\partial v^z}{\partial r}\bigg|_{r=R_1}\mathbf{e}_z=2\pi R_1 h\left[\mu\left(\frac{U}{2\mu}R_1+\frac{A}{R_1}\right)\right]\equiv F_d\mathbf{e_z}.$$

[2]Generally speaking, drag is the component of the reactional force of the fluid in the direction of the body motion, the perpendicular component being called the lift. As we are concerned with one-dimensional motion of the body and no lift is involved due to the symmetry of the problem, we can distinguish between the effect of the pressure and the viscous forces, the latter not being present at rest.

Substituting the definition of A, we get

$$F_d = \pi h \left\{ U R_1^2 + \frac{2\mu}{\ln \frac{R_1}{R_2}} \left[v^* - \frac{U}{4\mu}(R_1^2 - R_2^2) \right] \right\} =$$

$$= \pi h \left[\frac{2\mu v^*}{\ln \frac{R_1}{R_2}} + U \left(R_1^2 - \frac{R_1^2 - R_2^2}{2 \ln \frac{R_1}{R_2}} \right) \right].$$

Using (2.3), the expression can be further manipulated to obtain

$$F_d = 2\pi h \left[\frac{\mu v^*}{\ln \frac{R_1}{R_2}} \right.$$

$$\left. + \frac{4\mu v^*}{R_1^2 - R_2^2 - (R_1^2 + R_2^2) \ln \frac{R_1}{R_2}} \left(\frac{R_1^2}{2} - \frac{R_1^2 - R_2^2}{4 \ln \frac{R_1}{R_2}} \right) \right]$$

$$= 2\pi h \mu v^* \frac{R_1^2 - R_2^2 - (R_1^2 + R_2^2) \ln \frac{R_1}{R_2} + \left(2R_1^2 \ln \frac{R_1}{R_2} - R_1^2 + R_2^2 \right)}{\left[R_1^2 - R_2^2 - (R_1^2 + R_2^2) \ln \frac{R_1}{R_2} \right] \ln \frac{R_1}{R_2}}$$

$$= 2\pi h \mu v^* \frac{(R_1^2 - R_2^2) \ln \frac{R_1}{R_2}}{\left[R_1^2 - R_2^2 - (R_1^2 + R_2^2) \ln \frac{R_1}{R_2} \right] \ln \frac{R_1}{R_2}}.$$

Returning back to U, we can write the drag in an compact form

$$F_d = \pi h \frac{U}{2}(R_1^2 - R_2^2). \tag{2.5}$$

With respect to sign convention (z axis oriented upwards) the equation of motion for the sinker (1.3) is stated as

$$m_s \frac{\mathrm{d}v^*}{\mathrm{d}t} = -m_s g + F_b + F_d;$$

using (2.4) and (2.5) the equation takes the form

$$m_s \frac{\mathrm{d}v^*}{\mathrm{d}t} = -m_s g + \pi R_1^2 h(\rho_f g - U) + \pi h \frac{U}{2}(R_1^2 - R_2^2),$$

$$\rho_s \frac{\mathrm{d}v^*}{\mathrm{d}t} = g(\rho_f - \rho_s) - \frac{U}{2R_1^2}(R_1^2 + R_2^2).$$

The sinker attains the terminal velocity if $\frac{\mathrm{d}v^*}{\mathrm{d}t} = 0$. Then

$$U = g(\rho_f - \rho_s) \frac{2R_1^2}{R_1^2 + R_2^2},$$

and, substituting (2.3) again,

$$4\mu v^* = g(\rho_f - \rho_s) \frac{2R_1^2 \left(R_1^2 - R_2^2 - (R_1^2 + R_2^2) \ln \frac{R_1}{R_2} \right)}{R_1^2 + R_2^2},$$

we obtain the formula for *terminal velocity* in the well-known form

$$v^*_{term} = \frac{g(\rho_f - \rho_s)}{2\mu} \frac{R_1^2 \left(R_1^2 - R_2^2 - (R_1^2 + R_2^2) \ln \frac{R_1}{R_2} \right)}{R_1^2 + R_2^2}. \tag{2.6}$$

Alternative derivations can be found in [19] and [20].

3. Technical details of the computation

The finite element code used for the computations presented further on was developed by J. Hron in 2001 [21]. The code was employed in several studies concerning flows of incompressible Newtonian and non-Newtonian fluids, including piezoviscous ones [22], [11], [23]. The works cited used a viscosity model including dependence on the shear rate

$$\mu(p, |\mathbb{D}|^2).$$

Calculation of incompressible flows with pressure-dependent viscosity is generally a challenging task; the pressure-viscosity coefficient β must be low enough to achieve a convergence in the nonlinear method (for instance, a condition $\beta < 10^{-3}$ was found in [22]).

Let us now briefly describe the basic features of the numerical method. The flow equations in the weak formulation[1]

$$\left(\frac{\partial \mathbf{v}}{\partial t}, \mathbf{w}\right) + (\mathbf{v}\cdot\nabla\mathbf{v}, \mathbf{w}) - (p, \nabla\cdot\mathbf{w}) + (\mathbb{T}, \nabla\mathbf{w}) = (\mathbf{f}, \mathbf{w}) + \langle \mathbb{T}\mathbf{n}, \mathbf{w}\rangle_{\Gamma_N} \qquad \forall \mathbf{w} \in \mathbf{X},$$

$$(\nabla\cdot\mathbf{v}, q) = 0 \qquad \forall q \in Y,$$

are spatially discretized using quadrilateral Stokes element pair Q^2/P^1_{disc}. The discrete spaces are defined as

$$\mathbf{X}_h = \{\mathbf{v} \in \mathbf{W}^{1,2}(\tilde{\Omega}), \hat{\mathbf{v}}|_{\hat{K}} \in \mathbf{Q}^2 \,\forall K \in \mathcal{T}_h\},$$

$$Y_h = \{p \in L^2(\tilde{\Omega}), \hat{p}|_{\hat{K}} \in P^1 \,\forall K \in \mathcal{T}_h\};$$

the velocity is approximated by biquadratic functions on the reference element $\hat{K} = (-1, 1)^2$, i. e.

$$Q^2(\hat{K}) = \text{span}\left\{1, x, x^2, y, y^2, xy, xy^2, x^2y, x^2y^2\right\},$$

the pressure is approximated by a linear function on each reference element and is generally discontinuous. The Q^2/P^1_{disc} pair is stable in the sense of satisfying the discrete inf-sup condition [24]. Backward (implicit) Euler method is used for the temporal discretization, approximating the time derivative at t^n as

$$\frac{\partial \mathbf{v}}{\partial t} \approx \frac{\mathbf{v}^{n+1} - \mathbf{v}^n}{\Delta t}.$$

A nonlinear set of equations for the discrete velocity $\boldsymbol{v}$ and pressure $\boldsymbol{p}$

$$\mathbf{C}(\boldsymbol{v}) + \mathbf{D}(\boldsymbol{v}, \boldsymbol{p}) - \mathbf{G}(\boldsymbol{p}) - \boldsymbol{f} = \mathbf{0}, \tag{3.1a}$$

$$\mathbf{G}^\dagger(\boldsymbol{v}) = \mathbf{0}, \tag{3.1b}$$

$$\boldsymbol{\Gamma}(\boldsymbol{v}, \boldsymbol{p}) = \mathbf{0} \tag{3.1c}$$

[1] $(\mathbf{a}, \mathbf{b}) = \int_{\tilde{\Omega}} \mathbf{a}\cdot\mathbf{b}\,\mathrm{d}x$

is to be solved at each time level, $\mathbf{C}$ being the approximation of the convective operator $(\mathbf{v}\cdot\nabla)\mathbf{v}$, $\mathbf{D}$ the approximation of the viscous term

$$\int_\Omega 2\mu(p)\mathbb{D}(\mathbf{v}) : \mathbb{D}(\mathbf{w})\ \mathrm{d}x.$$

$\mathbf{G}$, $\mathbf{G}^\dagger$ correspond to discrete approximations of the gradient and divergence respectively, and $\mathbf{\Gamma}$ accounts for the boundary conditions.

The solution of the coupled system (3.1) is then sought via Newton-Raphson method with line-search as the root of the discrete equation residue $\tilde{\Phi}(\boldsymbol{v},\boldsymbol{p})$

$$[\boldsymbol{v},\boldsymbol{p}]^{n+1} = [\boldsymbol{v},\boldsymbol{p}]^n + \omega^n \left(\frac{\partial\tilde{\Phi}(\boldsymbol{v},\boldsymbol{p})}{\partial[\boldsymbol{v},\boldsymbol{p}]}\right)^{-1} \tilde{\Phi}(\boldsymbol{v},\boldsymbol{p})$$

The Jacobian matrix $\frac{\partial\tilde{\Phi}(\boldsymbol{v},\boldsymbol{p})}{\partial[\boldsymbol{v},\boldsymbol{p}]}$ is approximated by finite difference and its inverse is computed directly through LU decomposition as implemented in the *UMFPACK* package [25].

4. Planar flows of piezoviscous fluids

To check the finite element code for the capability of calculaing piezoviscous flows, we performed a series of calculations of planar steady flows of piezoviscous liquids with constituive relation

$$\mu = \alpha\mu_0 p = ap, \tag{4.1}$$

for which analytical solutions exist. As shown in [22] and [26], the linear models (4.1) and (1.14) are the only ones which admit a solution in a form of *unidirectional flow* in two space dimensions.

4.1 Computational domain and boundary conditions

We will now discuss flows in a planar channel $[x, y] \subset \mathbb{R}^2; y \in (-1, 1)$.

To solve the problem numerically using finite element method, we introduce a rectangular mesh depicted in Figure 4.1. The left-bottom corner is located at $[0, -1]$, the right-top at $[20, 1]$. By d we will denote the length of the channel.

The initial mesh consisted of 40 square elements; one step of mesh refinement divides each element into four. Each side of the rectangle $(0, 20) \times (-1, 1)$, representing the computational domain, has different boundary condition for v_x prescribed:

- **-8** (left vertical side, inflow): Stress boundary condition, analytical pressure is prescribed: $\mathbf{n} \cdot \mathbb{T}\mathbf{n} = \hat{p}(x, y)|_{x=0}$.
- **-2** (right vertical side, outflow): Stress condition, analytical pressure: $\mathbf{n} \cdot \mathbb{T}\mathbf{n} = \hat{p}(x, y)|_{x=L}$
- **-1** (bottom horizontal side): Dirichlet boundary, $v_x = 0$.
- **-7** (top horizontal side): Dirichlet boundary, $v_x = v_{bcv}$

The $y-$component of the velocity is constrained to $v_y = 0$ at the whole boundary.

The Poiseuille and Poiseuille-Couette flows are characterized by two constants, determining the boundary conditions. These constants, provided to the nonlinear solver by a configurational file together with the material parameters, are as follows:

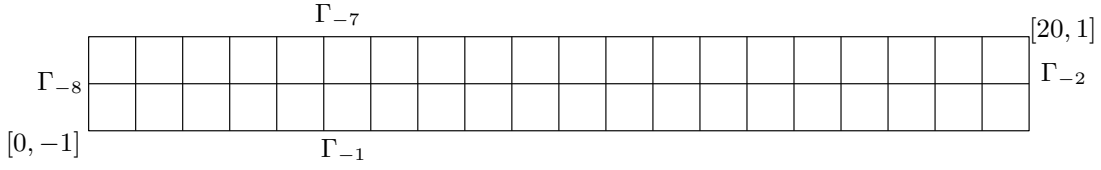

Figure 4.1: The computational domain for planar flows of liquids with pressure-dependent viscosity.

- v_{bcv}, the speed of the upper plate.
- p_{in}, the inflow pressure at the centre of the inflow boundary (-8).

The ouflow pressure is set to $p_{out} = 1$.

4.1.1 Initialization of the nonlinear solver

Since the flows examined are steady, there is no need for an initial condition. However, a nonlinear iterative solver needs a good starting approximation to work efficiently. For the planar flows described below, we prescribed the analytical pressure and velocity fileds as an inital guess. Another option is to input the pressure and velocity field akin to the flow of a Newtonian fluid established by desired pressure drop. Both ways ensure positive value of the viscosity; this is crucial for the discrete system Jacobian $\frac{\partial \Phi(\boldsymbol{v},\boldsymbol{p})}{\partial [\boldsymbol{v},\boldsymbol{p}]}$ to be invertible.

4.2 Poiseuille flow

A flow in a straight channel induced by applied pressure gradient is usually referred to as planar Poiseuille flow. An analytical solution to the nondimensionalised equations is derived in [22] for the model (4.1):

$$\hat{v}_x(y) = \frac{1}{a} \log \left(\frac{\cosh c_0 y}{\cosh c_0} \right), \tag{4.2a}$$

$$\hat{p}(x,y) = L \cosh(c_0 y) \exp(c_0 x); \quad y \in \langle -1, 1 \rangle . \tag{4.2b}$$

The constant c_0, which characterises the flow, is intimately related to the pressure gradient. We can set $c_0 = \frac{1}{d} \ln \left(\frac{p_{out}}{p_{in}} \right)$ in order to match pressure drop in the direction of the x axis. The walls are fixed, so we set $v_{bcv} = 0$. L is chosen so as to satisfy $\hat{p}(0,0) = p_{in}$ at the inflow; since $p_{out} = 1$, $L = p_{in}$. Therefore, for arbitrary values of p_{in} are the constants of the analytical solution uniquely determined.

Table 4.1 shows the L^2-norms of the FEM solution error for two different values of c_0. One can see that per one step of regular mesh refinement (reducing h by half) the pressure error diminishes by a factor of four and the velocity by a factor of eight; while the rate of convergence for the velocity is of order three, the pressure rate of convergence is of order two, as expected in [24].

Figures 4.2 – 4.4 give a brief graphical description of the velocity and pressure fields. Note that the exponential pressure drop in the flow calls for a plot in logarithmic scale. While the pressure increases dramatically with increasing c_0, the velocity varies only slightly. In fact, this holds for piezoviscous flows in general; such a phenomenon is called *choking*. It is widely recognized in processing fluids with significant dependence of the viscosity on the pressure [27].

refinement lev.	$\|\|p-\hat{p}\|\|_0$	$\|\|\mathbf{v}-\hat{\mathbf{v}}\|\|_0$	$\|\|\nabla\mathbf{v}-\nabla\hat{\mathbf{v}}\|\|_0$
$c_0 = -0.0269,\ a = 3.75$			
0	5.705592e-04	1.052443e-06	6.142751e-06
1	1.421551e-04	1.034549e-07	1.363057e-06
2	3.552805e-05	1.026312e-08	2.820415e-07
3	8.884510e-06	2.204945e-09	5.969051e-08
4	2.232765e-06	1.960952e-09	1.354276e-08
5	6.029216e-07	1.959135e-09	4.346297e-09
$c_0 = 0.5,\ a = 1$			
0	4.584602e+02	5.327424e-03	3.115210e-02
1	1.166972e+02	5.785380e-04	7.370067e-03
2	2.928669e+01	6.918441e-05	1.789106e-03
3	7.328305e+00	8.544160e-06	4.428879e-04
4	1.832477e+00	1.064609e-06	1.103993e-04
5	4.581438e-01	1.329612e-07	2.757594e-05

Table 4.1: The L^2-norms of the errors from the analytical solution $[\hat{p}, \hat{\mathbf{v}}]$ of the planar Poiseuille flow.

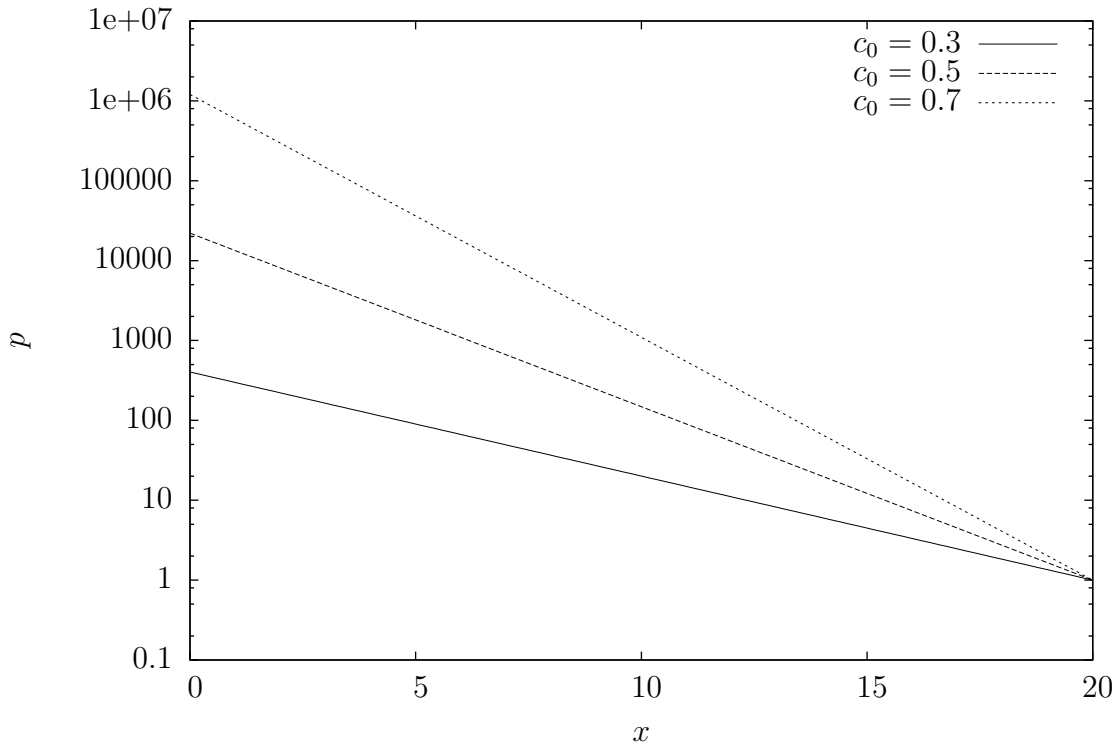

Figure 4.2: The pressure along the x axis for the plane Poiseuille flow, $a = 1$.

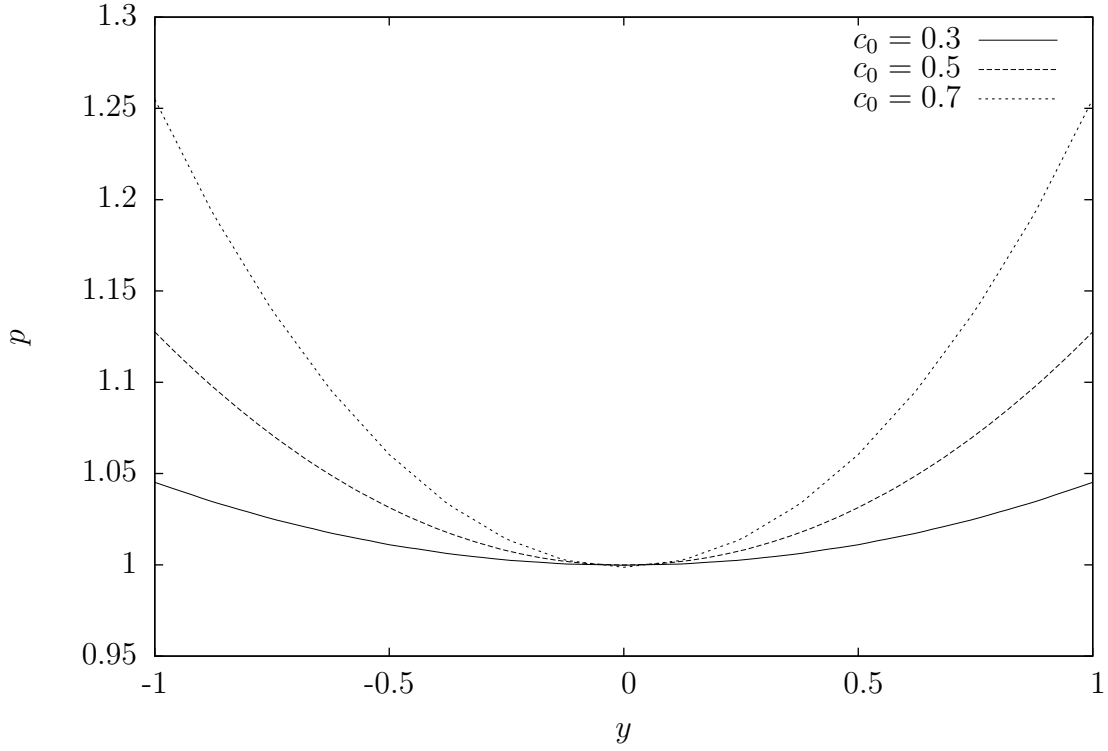

Figure 4.3: Planar Poiseuille flow, the pressure at the outflow boundary.

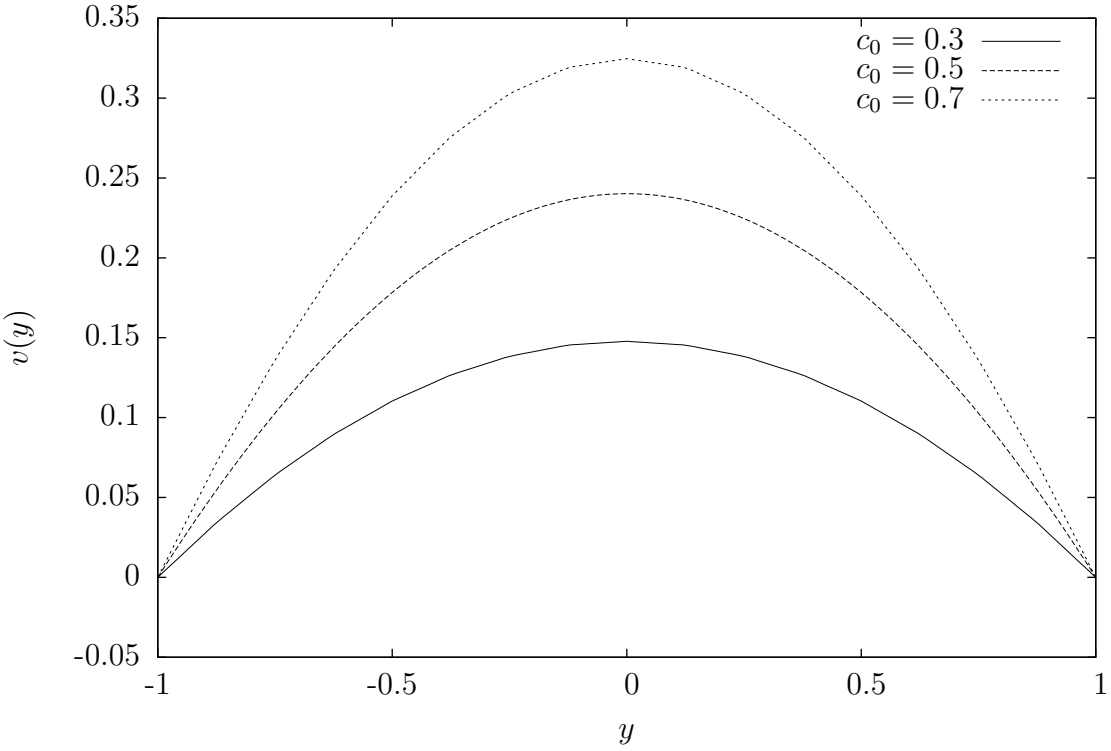

Figure 4.4: The velocity profile for the plane Poiseuille flow, $a = 1$.

refinement lev.	$\|\|p-\hat{p}\|\|_0$	$\|\|\mathbf{v}-\hat{\mathbf{v}}\|\|_0$	$\|\|\nabla\mathbf{v}-\nabla\hat{\mathbf{v}}\|\|_0$
$c_0 = 0.5,\ a = 1,\ M = 2$			
0	5.103657e+02	5.803250e-03	8.298749e-02
1	1.300277e+02	6.637285e-04	1.992583e-02
2	3.261273e+01	8.073154e-05	4.329300e-03
3	8.157538e+00	1.033270e-05	

Table 4.2: The L^2-norms of the errors from the analytical solution $[\hat{p}, \hat{\mathbf{v}}]$ for the two-dimensional Poiseuille-Couette flow.

4.3 Poiseuille-Couette flow

We call a two-dimensional flow between parallel plates moving with constant speed with applied pressure gradient *Poiseuille-Couette flow*[1]. The analytical solution takes the form [22]

$$p(x,y) = L\left[M\exp(2c_0 y) + 1\right]\exp\left(c_0(x-y)\right), \tag{4.3a}$$

$$v_x(y) = \int_{-1}^{y} \frac{1}{a}\frac{M\exp(c_0 y) - 1}{M\exp(c_0 y) + 1}\,\mathrm{d}y. \tag{4.3b}$$

with c_0, M, L as the constants of integration.

Using c_0, we are able to compute M from (4.3a) so as to satisfy the boundary condition for the velocity at $y = 1$. Then one gets the value of L by requiring the inflow pressure at the centre to be equal to p_{in}. In fact, we choose reasonable values for M and c_0 first (in our example, $c_0 = 0.5$ and $M = 2$) and compute p_{in}, v_{bcv} via (4.3a) and (4.3b), respectively, afterwards.

The integral errors form analytical solution are shown in Table 4.3, velocity and pressure profiles in Figures 4.5–4.6.

4.4 Poiseuille flow in a circular pipe

An analytical solution can be constructed for a Poiseuille flow in a circular pipe when the viscosity of the fluid depends on the pressure through Barus law

$$\mu = \mu_0 \exp[\beta(p - p_0)].$$

The solution was published by Denn [27] in 1981; the velocity and the pressure are expressed in terms of Δp_0 – the pressure drop which would result in a flow with $[\mathbf{v}_0, p_0]$ if the fluid were Newtonian with viscosity μ_0.

Interestingly enough, the velocity profile is found to be parabolic

$$\hat{\mathbf{v}}(r) = \frac{1}{4\mu_0}\frac{\Delta p_0}{L}\left(r^2 - R^2\right)\mathbf{e}_z, \tag{4.4}$$

and the pressure has the form

$$\hat{p}(r,z) = \tilde{p} - \frac{1}{\beta}\ln\left[1 - \beta\Delta p_0 e^{\beta\tilde{p}}\left(1 - \frac{z}{L}\right)\right] + \frac{1}{\beta}\ln\left[\frac{2 - 2\sqrt{1-\xi^2(r,z)}}{\xi^2(r,z)}\right], \tag{4.5}$$

[1]There is a difference between a Poiseuille-Couette and the Couette-Poiseuille flow [28]; in the former, studied in the present work, the flow is driven mainly by the pressure drop. There is no point in studying pure (planar) Couette flow, as the pressure (and, consequently, the viscosity) is constant.

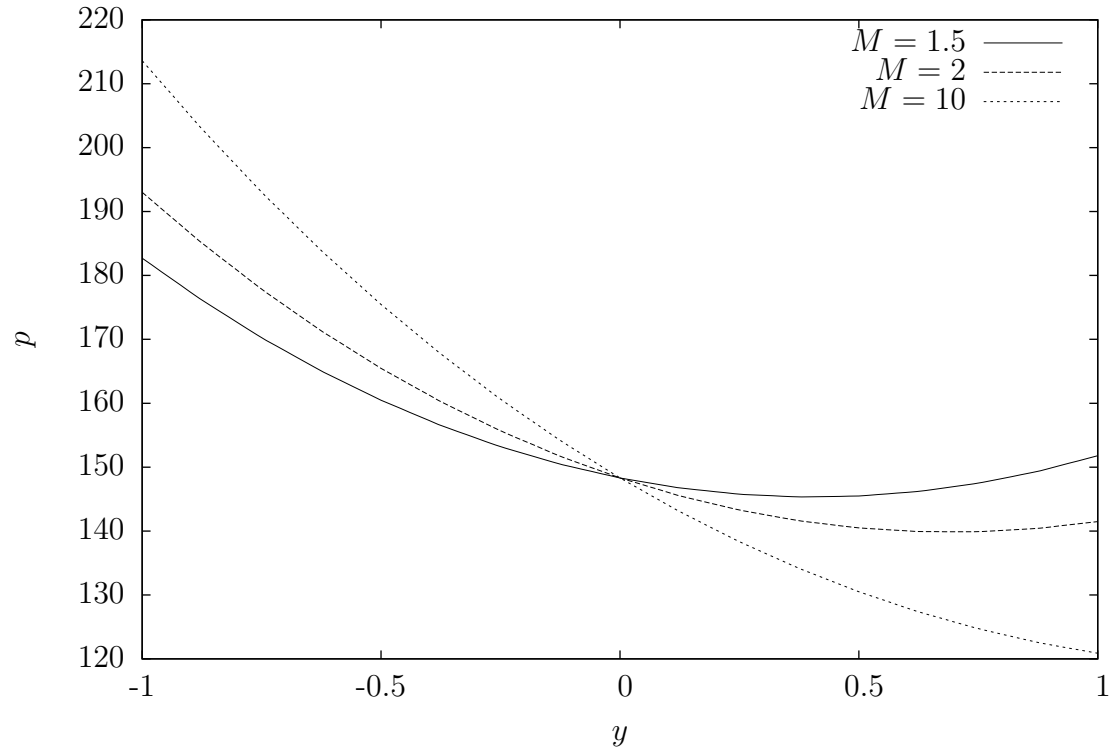

Figure 4.5: Transversal view of the pressure for the two-dimensional Poiseuille-Couette flow, $a = 1,\ c_0 = -0.5$

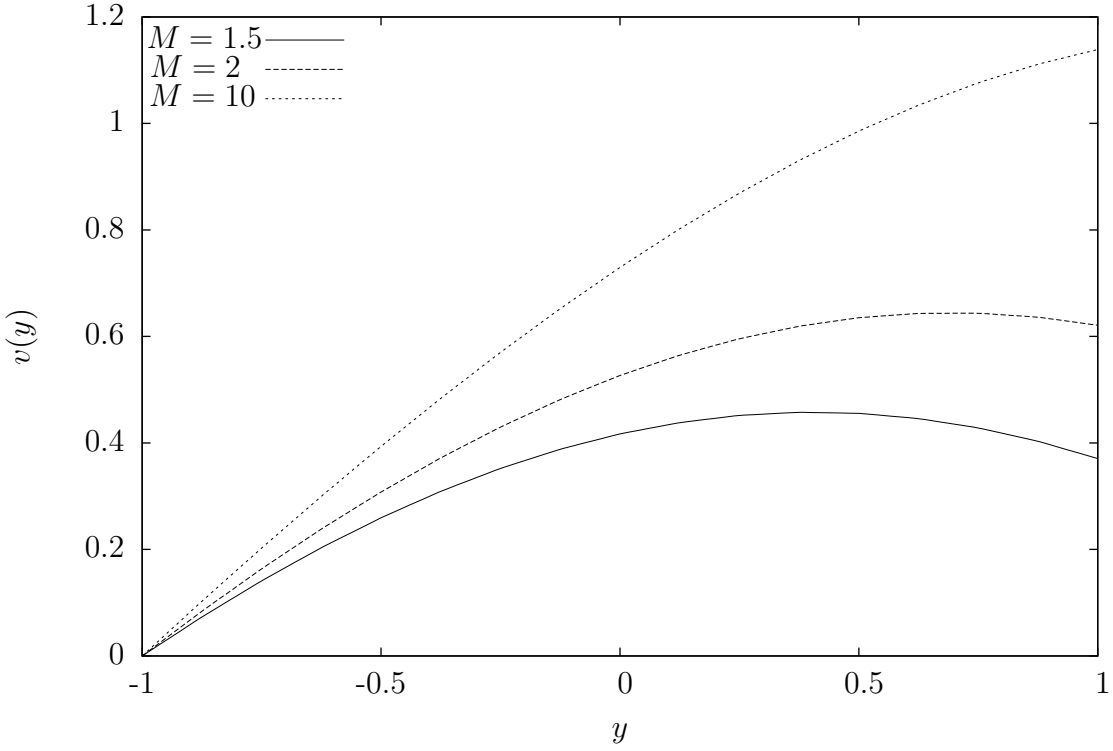

Figure 4.6: The velocity profile for the two-dimensional Poiseuille-Couette flow, $a = 1,\ c_0 = -0.5$.

where $\xi(r,z)$ is introduced as

$$\xi(r,z) = \frac{\beta\Delta p_0 e^{\beta\tilde{p}}\left(\frac{r}{R}\right)}{1-\beta\Delta p_0 e^{\beta\tilde{p}}\left(1-\frac{z}{L}\right)}\left(\frac{R}{L}\right).$$

$\tilde{p}$ in the equations above represents the outflow pressure in the centre of pipe cross section; its value was set to zero in our calculations.

Numerical solution of the flow

The cylindrical symmetry of the problem allowed us to drop any dependence on the azimuthal coordinate φ, reducing the computational problem to two spatial dimensions. Due to the unidirectionality of the flow, resulting in $v^r \equiv 0$ in Ω , we were able to formulate the flow equations in terms of the system residue Φ as follows:

$$\Phi_{\boldsymbol{p}}(\mathbf{v};q) = \int \left(r\frac{\partial v^z}{\partial z} + r\frac{\partial v^r}{\partial r} + v^r\right) q \ \mathrm{d}r \ \mathrm{d}z, \tag{4.6a}$$

$$\begin{aligned}\Phi_{\boldsymbol{v}^r}(\mathbf{v},p;\boldsymbol{\varphi}) = \\ \int \left[r\left(v^z\frac{\partial v^r}{\partial z} + v^r\frac{\partial v^r}{\partial r}\right) - p + 2\mu\frac{v^r}{r}\right]\varphi^r \\ + r\left(-p+2\mu\frac{\partial v^r}{\partial r}\right)\frac{\partial\varphi^r}{\partial r} + r\mu\left(\frac{\partial v^r}{\partial r}+\frac{\partial v^z}{\partial z}\right)\frac{\partial\varphi^r}{\partial z}\ \mathrm{d}r\ \mathrm{d}z,\end{aligned} \tag{4.6b}$$

$$\begin{aligned}\Phi_{\boldsymbol{v}^z}(\mathbf{v},p;\boldsymbol{\varphi}) = \int r\left(v^z\frac{\partial v^z}{\partial z} + v^r\frac{\partial v^z}{\partial r}\right)\varphi^z \\ + r\mu\left(\frac{\partial v^r}{\partial r}+\frac{\partial v^z}{\partial z}\right)\frac{\partial\varphi^z}{\partial r} + r\left[-p+\left(2\mu\frac{\partial v^z}{\partial z}\right)\right]\frac{\partial\varphi^z}{\partial z}\ \mathrm{d}r\ \mathrm{d}z.\end{aligned} \tag{4.6c}$$

The computational domain was rectangular as in the case of planar flows (Fig. 4.1); the boundary notation from the 2D computations was preserved as well. We chose $R = 4$, $L = 20$ for our numerical experiments. The initial mesh consisted of 80 square elements.

The Dirichlet condition $\mathbf{v} = \mathbf{0}$ was prescribed on Γ_{-7}, representing the tube wall. Both the inflow and outflow were implemented as the Neumann-type boundary condition, prescribing the analytical pressure

$$\mathbb{T}\mathbf{n} = \hat{p}(r,z)\mathbf{n}.$$

When dealing with flows with circular symmetry, most cumbersome is to prescribe appropriate conditions at the axis of symmetry that do not affect the flow. The geometry of the problem implies

$$v^r = 0, \tag{4.7a}$$

$$\frac{\partial v^z}{\partial r} = 0, \tag{4.7b}$$

at $r = 0$. Actually, it is possible to require the symmetry in the sense of natural boundary condition

$$(\mathbb{T}\mathbf{n})\mathbf{n} = 0, \tag{4.8}$$

$R = 4,$	$L = 20,$	
$\rho_f = 1,$	$\mu_0 = 20,$	$\beta = 10^{-4},$
Δp_0:		
	$4 \cdot 10^3$	
	$5 \cdot 10^3$	
	$6 \cdot 10^3$	

Table 4.3: Parameter values for the numerical solution of a piezoviscous Poiseuille flow in a pipe.

refinement lev.	$\|\|p - \hat{p}\|\|_0$	$\|\|\mathbf{v} - \hat{\mathbf{v}}\|\|_0$
0	7.442807e+00	9.512327e-04
1	1.865672e+00	7.074131e-05
2	4.667764e-01	5.300944e-06
3	1.167186e-01	4.111396e-07
4	2.918132e-02	3.318647e-08

Table 4.4: The L^2-norms of the errors from the analytical solution $[\hat{p}, \hat{\mathbf{v}}]$ for the Poiseuille flow in a circular pipe of radius $R = 4$. β =1e-4,$\mu_0 = 20$, Δp_0 =5e3.

merely requiring there is no transversal stress at the axis of symmetry. Still, the constraint (4.7a) needs to be supplied in the sense of the Dirichlet condition. Instead of using the stress condition (4.8), we managed to force the symmetry completely in the sense of Dirichlet boundary condition, prescribing (4.7a) for the r-component of the momentum balance and (4.7b) for the z-component. See also Section 5.5.2 for a brief discussion of the symmetry conditions.

For various values of U, μ_0, β we checked the L^2 norms of the error of the finite element solution from the analytical $[\hat{p},\ \hat{\mathbf{v}}]$ given by (4.5), (4.4) and also the volumetric flow predicted by Hagen-Poiseuille law

$$Q = \frac{\pi R^4}{8\mu_0} \frac{\Delta p_0}{L};$$

note that since the velocity is determined by Δp_0, the volumetric flow is the same for both the Newtonian and piezoviscous case. We observed that for given Δp_0 the value of β must be such that the condition

$$\beta \Delta p_0 \lesssim 1 \tag{4.9}$$

holds in order to attain convergence in the Newton method. Table 4.3 sums up the values of parameters used in the computations.

Table 4.4 illustrates the rate of convergence for the finite element solution. The velocity profile, downstream evolution of the pressure in the pipe and radial change of the pressure are shown in Figures 4.7-4.9.

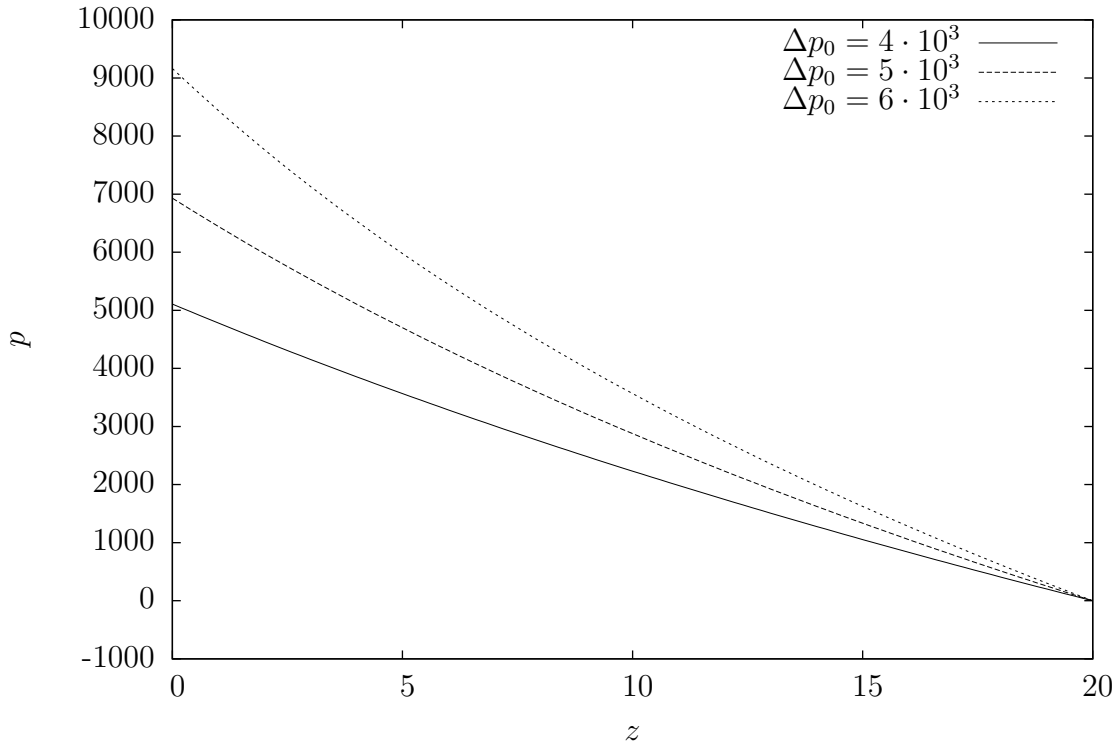

Figure 4.7: The pressure profile along the flow for the piezoviscous Poiseuille flow in a pipe. Refer to Table 4.3 for parameter values.

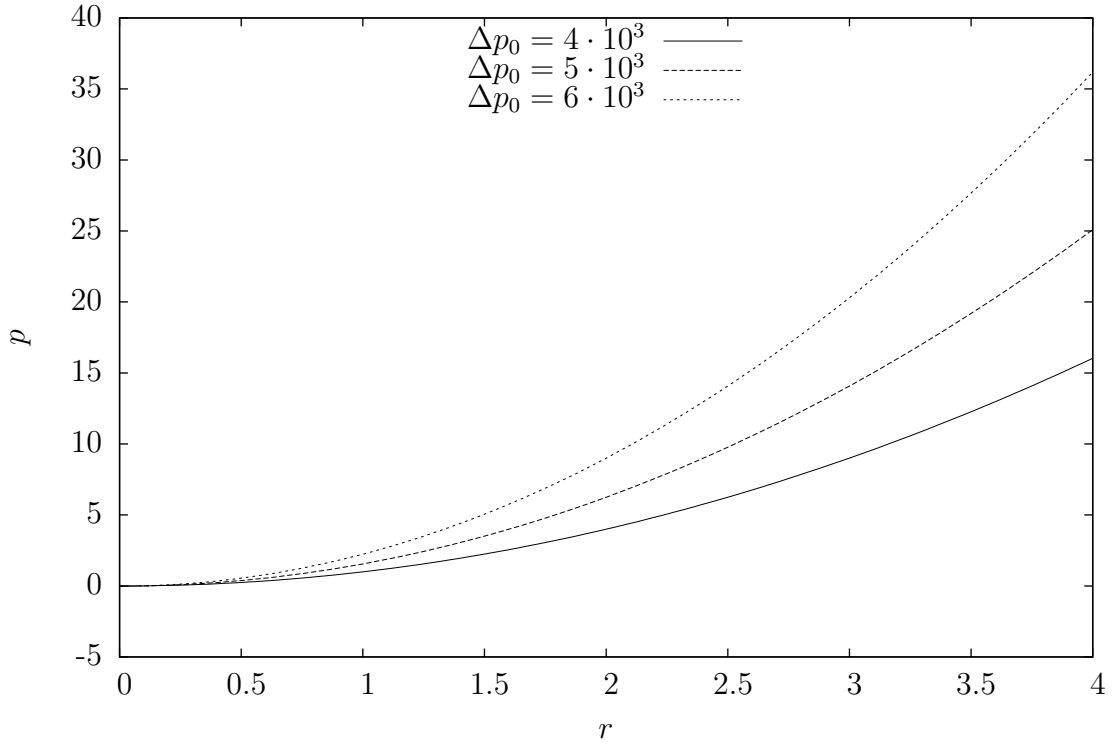

Figure 4.8: The pressure profile along the pipe radius at the outflow boundary for the piezoviscous Poiseuille flow. Refer to Table 4.3 for parameter values.

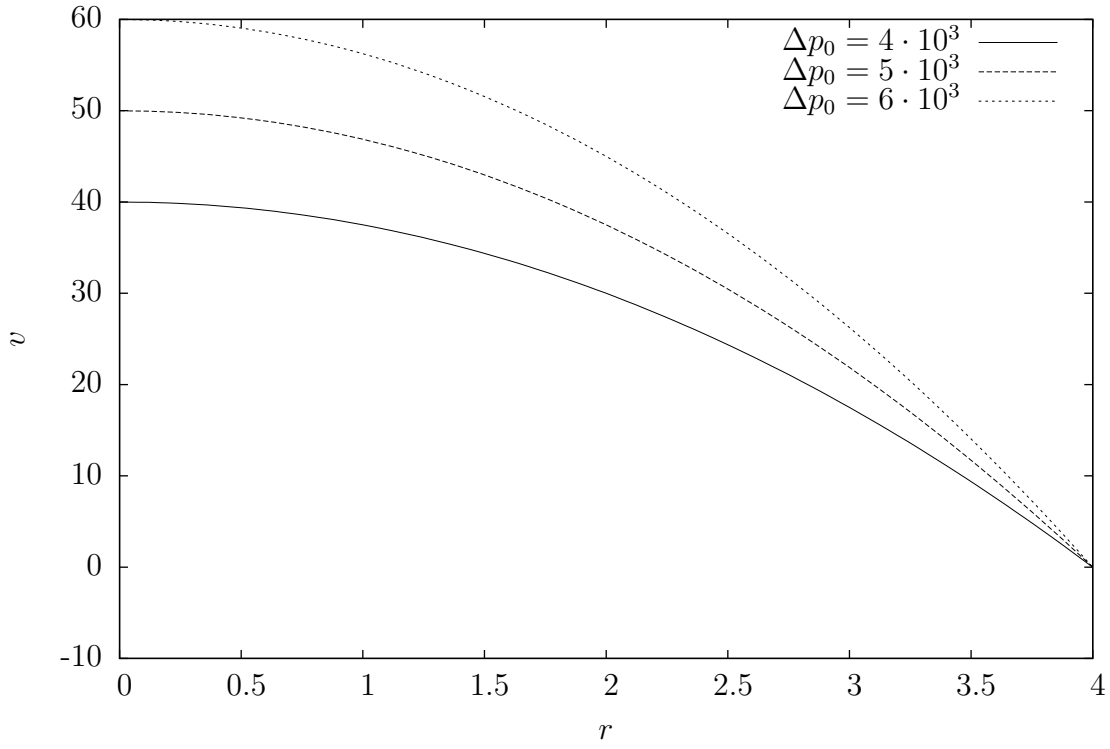

Figure 4.9: The parabolic velocity profile of the piezoviscous Poiseuille flow in a pipe. Refer to Table 4.3 for parameter values.

5. Fall of a rectangle in an infinite channel

5.1 Global coordinate transform

One of the ways to cope with the motion of a rigid body in a fluid is to perform a coordinate transform.

The problem of sinker motion in a stationary fluid can be transformed by changing the frame of reference

$$t \to \bar{t} = t$$

$$\mathbf{x} \to \bar{\mathbf{x}} = \mathbf{x} - \int_0^t v^*(t)\mathbf{e}_z \, \mathrm{d}t.$$

The balance of mass is stated the same as in laboratory frame of reference:

$$\bar{\nabla} \cdot \bar{\mathbf{v}} = 0.$$

Fluid velocity with respect to the body $\bar{\mathbf{v}}$ is "shifted" against $\mathbf{v}$ by $v^*(t)\mathbf{e}_z$ and we have to take into account acceleration of the sinker $\frac{\mathrm{d}v^*}{\mathrm{d}t}$ as well. The transformation is not Galilean, so the balance of linear momentum in the new frame of reference takes the form

$$\rho_f \left[\frac{\partial \bar{\mathbf{v}}}{\partial t} + (\bar{\mathbf{v}} \cdot \bar{\nabla})\bar{\mathbf{v}} \right] = \bar{\nabla} \cdot \bar{\mathbb{T}} - \rho_f g \mathbf{e}_z - \rho_f \frac{\mathrm{d}v^*}{\mathrm{d}t}\mathbf{e}_z. \quad \bar{\mathbf{x}} \in \bar{\Omega}.$$

All calculations addressed later will be performed in the frame of reference attached to the sinker and the bars over the quantities above will be dropped for the sake of simplicity.

5.2 Terminal velocity

Consider a rectangle of width 2Σ, length d, made from a homogeneous material of density[1] ρ_b falling in a infinite channel filled with a fluid of density ρ_f and constant viscosity μ. We assume the rectangle to be perfectly centered during the fall; the distance of the vertical sides from the channel walls will be denoted by b. The problem geometry is depicted in Figure 5.1. Let us now derive the expression for terminal velocity. With creeping motion of the fluid past the rectangle assumed, the solution to the flow equations in the gap on the right[2] can be expressed as

$$v_z(x) = \frac{U}{2\mu}(x - \Sigma)^2 + A(x - \Sigma) + B \tag{5.1a}$$

$$p(z) = (U - \rho_f g)z + C. \tag{5.1b}$$

[1] Two dimensional analogues of the material parameters will be considered. Even though they are of importance in surface physics, the problem of planar motion of a rectangle is related to the original FCV problem only formally; therefore we do not pay a special attention to the choice of physical units in the subsequent numerical experiments.

[2] Due to the lateral symmetry we will consider half of the rectangle only.

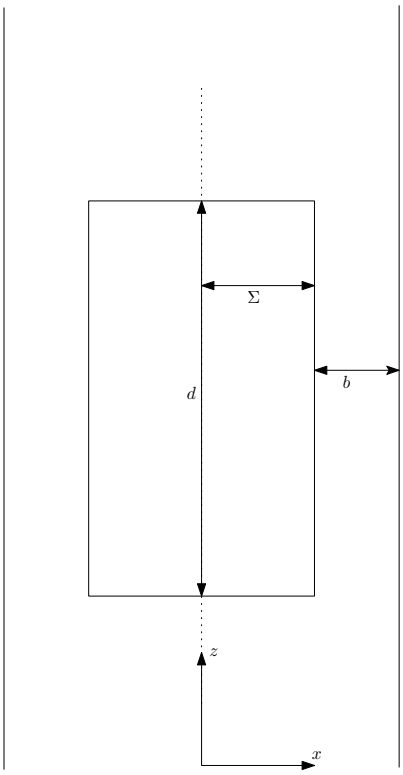

Figure 5.1: Dimensions of the 2D fall problem

The boundary conditions

$$\mathbf{v}|_{x=\Sigma} = \mathbf{0}, \quad \mathbf{v}|_{z=\Sigma+b} = \mathbf{v}_b$$

are accompained by the flux condition[3]

$$\int_0^R v_z(y)\mathrm{d}y = (b+\Sigma)v^*.$$

Solving for A,B, we get from the boundary conditions

$$B = 0, \quad A = \frac{v^*}{b} - \frac{Ub}{2\mu}.$$

The value of U is established from the flux condition, arriving at

$$U = -\frac{6\mu v^*}{b^3}\left(b + 2\Sigma\right). \tag{5.2}$$

Consequently, we can express A in terms of the problem constants as

$$A = v^* \frac{4b + 6\Sigma}{b^2}; \tag{5.3}$$

the drag on the vertical wall is given by

$$F_d = \int \mu \left.\frac{\partial v_z}{\partial x}\right|_{x=\Sigma} \mathrm{d}z = \mu v^* d \frac{4b + 6\Sigma}{b^2}. \tag{5.4}$$

[3]Note that the flow is described in the sinker frame of reference.

The buoyancy is

$$F_b = \Sigma(U - \rho_f g)d = -\frac{6\mu v^*}{\Sigma b^3}\left(b + 2\Sigma\right)d - \Sigma d\rho_f g. \tag{5.5}$$

The terminal velocity v^*_{term} is attained when the sum of the drag and the buyoancy equals the gravitational force

$$F_b(v^*) + F_d(v^*) = \Sigma d\rho_s g.$$

Finally, substituting for F_b, F_d and rearranging, v^*_{term} is given by

$$v^*_{term} = \frac{(\rho_f - \rho_s)g}{4\mu}\frac{\Sigma b^3}{b^2 + 3\Sigma b + 3\Sigma^2} \tag{5.6}$$

5.3 Flow in the gap – numerical solution

As an preliminary stage in the devisal of the method for the motion of a body, we calculated the flow in the gap numerically by prescribing the analytical velocity profile as the boundary condition, comparing the calculated drag to the value predicted by (5.4). The algorithm proceeded in two steps

1. Calculate the flow according to boundary conditions due to the body motion
2. Determine the body velocity v^* and position z^* from the forces calculated from the flow

This *decoupled* approach was used in subsequent simulations with changes made only to the numerical method. In the case of the 2D gap flow, an explicit Euler method was used to solve the equation of motion of the sinker. The algorithm can be written as follows:

Algorithm 1 The Euler metod as implemented in the flow in a gap.

$(z^*)^0 = 0$;
$(v^*)^0 = 0$
$(a^*)^0 = 10^{-10}$
while $|(a^*)^n| > 10^{-15}$ **do**
  solve NSE
  $F_b = \Sigma(p^n|_{z'=d} - p^n|_{z'=0})$
  $F_d = \int_0^d \mathbb{T}^n\mathbf{n}\ \mathrm{d}z'$
  $(a^*)^{n+1} = -g + \frac{1}{m_s}[F_d + F_b]$
  $(v^*)^{n+1} = (v^*)^n + (a^*)^{n+1}\Delta t$
  $(z^*)^{n+1} = (z^*)^n + (v^*)^{n+1}\Delta t$
end while

The drag $\int_\Gamma \mathbb{T}\mathbf{n}$ is calculated on the reference element using Gauss quadrature of fourth order. The velocity gradient is approximated using derivatives of the $Q^2(\hat{K})$ basis functions; the interpolation of the traction vector can be thus regarded as linear on the reference element (cf. Chapter 3.)

The mesh used for the flow calculation was taken from the piezoviscous flow tests described previously. Dirichlet boundary condition for the velocity given by

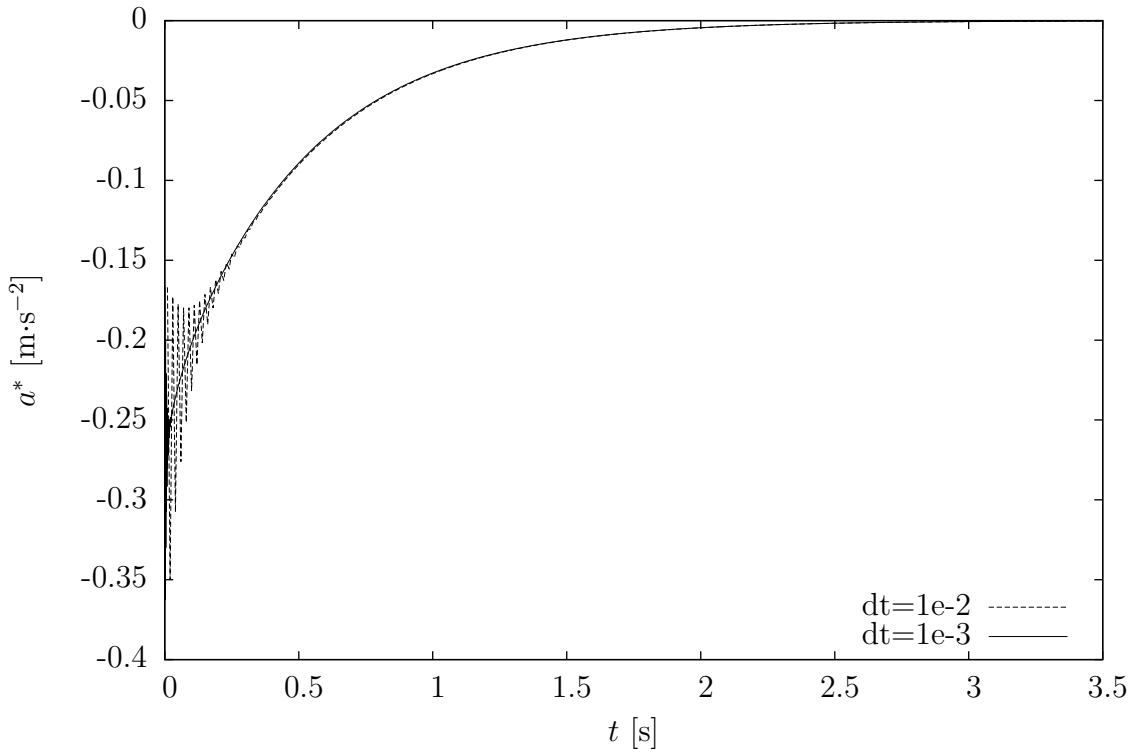

Figure 5.2: Time evolution of the accelarion of the falling plate. The occurence of oscillations for `dt`=1e-2 is a numerical artifact, which can be suppressed by decreasing the timestep.

(5.1a) is prescribed on boundaries Γ_{-7}, Γ_{-8}, with the constants of the solution U, A computed from (5.2–5.3) as the functions of $(v^*)^n$ at each time step. Stress condition $\mathbb{T}\mathbf{n} = (p_{conf} - \rho_f g(z^*)^n)\mathbf{n}$ was prescribed on Γ_{-2}. Time discretization of the flow equations was done using backward Euler method with the same time step value $\Delta t \equiv$`dt` as for the wall equation of motion.

Figure 5.2 shows the acceleration of the sinker $a^* \equiv \frac{\mathrm{d}v^*}{\mathrm{d}t}$ over time for two different timesteps. The equilibrium $a^* = 0$ is reached within the floating point precision (therefore a threshold slightly over machine epsilon $2.2 \cdot 10^{-16}$ was chosen as a stopping criterion for the calculation; in our example, the threshold was set at 10^{-15}.) The occurence of oscillations in the force after the release of a sinker is a consequence of the explicit Euler method employed. The one-step explicit method uses the values from the "old" timestep and tends to alternately over- and under-estimate the total force, leading to the behaviour observed. The oscillations decay far before the attainment of the terminal velocity and after 0.5 s they are not present any more; since we are primarily interested in the equilibrium state and the velocity does not seem to be affected by the oscillations (compare Fig. 5.3), making use of a multistep method would not make an observable difference. Figure 5.3 demonstrates that the terminal velocity (5.6) is attained precisely as all the end effects were avoided due to computational geometry. We also observe that the lines for two different timesteps nearly coincide as the drag F_d depends on velocity only.

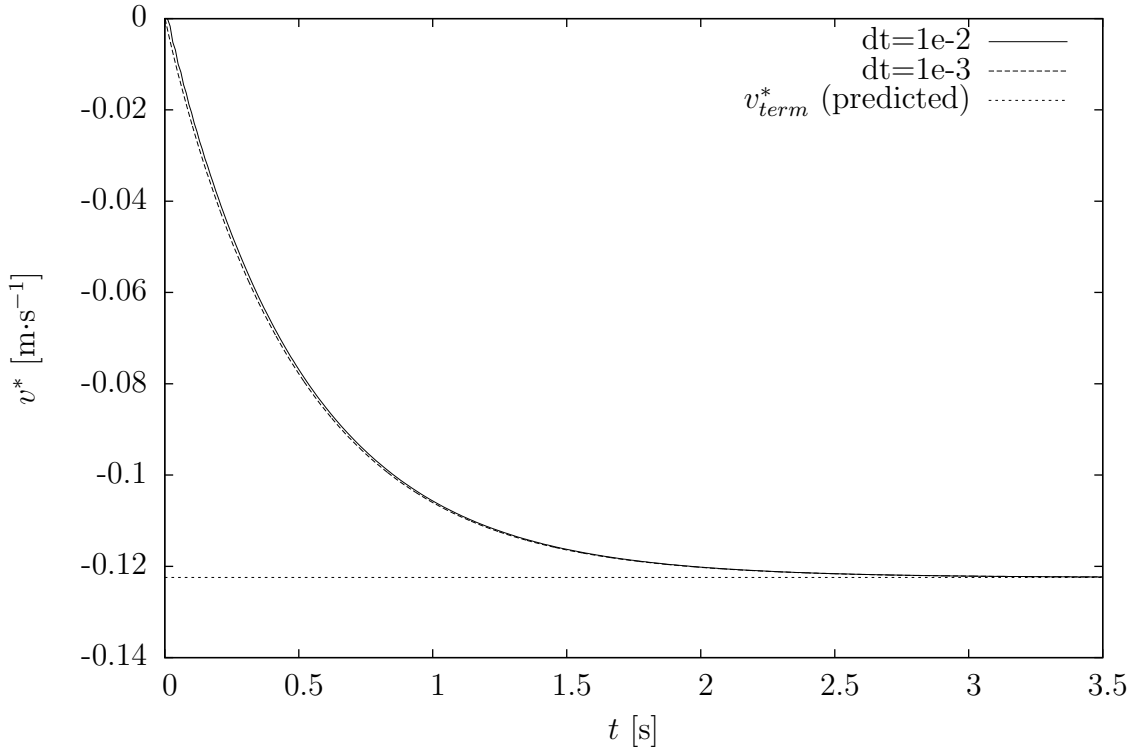

Figure 5.3: The speed of the falling plate over time; terminal velocity is calculated from (5.6).

5.4 The computational domain

Since the fluid far from the body should not be affected by the body motion, we examine a finite region only, prescribing appropirate conditions at the artificial boundaries. We also take the advantage of the frame of reference attached to the body; our problem is therefore set in a fixed finite domain. As can be seen in Figure 5.1, the problem posesses lateral symmetry, which assumes

$$v_x = 0, \tag{5.7}$$

$$\frac{\partial v_z}{\partial x} = 0, \tag{5.8}$$

at $x = 0$, cf. sec. 4.4. Hence we were led to simulate the problem in half of the domain only. A sketch of a mesh used for the computations is given in Figure 5.4.

The boundary of the domain is divided into 8 parts, numbered counterclockwise.

- Boundary **-8** is the inflow.
- Boundaries **-1** and **-5** coincide with the axis of symmetry of the problem.
- Boundaries **-2**,**-3**,**-4** represent the boundary of the sinker.
- Boundary **-6** is the outflow.
- Boundary **-7** represents the wall of the viscometer tube.

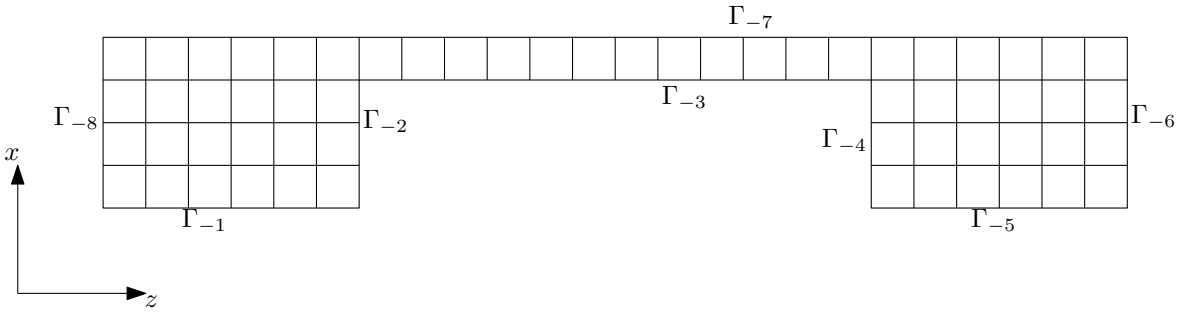

Figure 5.4: A sketch of the computational domain for simulations of the rectangle fall. The axes are rotated for easier view.

5.4.1 Lateral symmetry and the boundary conditions

Let us now discuss boundary conditions of the problem. Viewed from the sinker frame of reference, the outer wall is moving, while the sinker remains stationary. By virtue of the *no-slip* condition, we will prescribe Dirichlet-type boundary conditions as follows:

- $\mathbf{v} = -v^*\mathbf{e}_z$ at Γ_{-7},
- $\mathbf{v} = \mathbf{0}$ at $\Gamma_{-2} \cup \Gamma_{-3} \cup \Gamma_{-4}$.

The fluid sufficiently distant from the sinker is at rest in the laboratory frame of reference. Therefore, it is natural to prescribe

- $\mathbf{v} = -v^*\mathbf{e}_z$ at $\Gamma_{-8} \cup \Gamma_{-6}$.

However, we have another option for the boundary condition at the outflow. Following the approach of Rannacher *et al.* [29], we can prescribe the traction at Γ_{-6} as follows:

- $(\mathbb{T}\mathbf{n}) \cdot \mathbf{n} = p_{conf} - \rho_f g z_b$ for v^z,
- $v^x = 0$.

This choice ensures matching the pressure level at the outflow to desired value.

It still remains to choose an appropriate boundary condition fulfilling the symmetry. Different approaches were considered:

- *Dirichlet* approach: Prescribe (5.7) as the Dirichlet boundary condition for the v_x-equation. Add the constraint (5.8) to the equation for v_z.
- *Neumann* approach: Prescribe (5.7) as the Dirichlet condition for v^x. For v_z prescribe the natural boundary condition $(\mathbb{T}\mathbf{e}_x) \cdot \mathbf{e}_x = 0$. The condition is basically the free boundary condition.

It is also possible to enforce (5.8) by means of the natural boundary condition in the form $\mathbb{T}\mathbf{e}_x = -p\mathbf{e}_x + \mu\frac{\partial \mathbf{v}}{\partial x}$. (5.7) is then prescribed as the Dirichlet condition. Such a method was not considered in the subsequent calculations.

5.5 Force on the rectangle walls

In order to simulate the free fall problem properly, accurate evaluation of the forces acting on the body is essential. In accordance with (1.7), the total force on the "body" exerted by the fluid is decomposed into respective components pertaining to the boundary parts:

- Force on the Γ_{-2}, Γ_{-4} sides of the rectangle, facing the flow. In this part the pressure effects prevail.
- Force on the Γ_{-3} side oriented along the flow. This part accounts for the viscous forces.

We did a series of steady calculations for different values of the sinker velocity v^*, choosing $\Sigma = 3$ m, $b = 2$ m, $\rho_s = 2\ \mathrm{kg}\cdot\mathrm{m}^{-2}$, $\rho_f = 1\ \mathrm{kg}\cdot\mathrm{m}^{-2}$, $\mu = 1\ \mathrm{Pa}\cdot\mathrm{s}\cdot\mathrm{m}$, $g_z = 1\ \mathrm{m}\cdot\mathrm{s}^{-2}$ as the parameters. Assuming $v^*_{term} = -0.1224\ \mathrm{m}\cdot\mathrm{s}^{-1}$ as the characteristic velocity and b as the characteristic length, the Reynolds number is $\mathrm{Re} \approx 0.2$; the flow regime is laminar, though a narrower gap would lead to even smaller Reynolds number. We investigated the effect of the boundary conditions for the symmetry, mesh refinement levels and the free space left behind the sinker.

5.5.1 Effect of the free space left

The original problem is set in the infinite domain; it is important to make sure that the flow at the artificial boundaries $\Gamma_{-8,-6}$ does not have any impact on the fluid in the vicinity of the body. Figure 5.5 shows the total specific force (force per unit mass of the sinker) for velocities in the range $v^* \in (-0.1, 0)\ \mathrm{m}\cdot\mathrm{s}^{-1}$; terminal velocity for the geometry considered is $-0.1224\ \mathrm{m}\cdot\mathrm{s}^{-1}$. Note the linear dependence of the force on the velocity; the dependence of F_b, F_d on v^* is linear as well, cf. (5.5) and (5.4). All the points in Figures 5.5, 5.6 coincide, so we can assume that both Neumann- and Dirichlet-style of symmetry constraint are equivalent and that 40 m is enough space to leave behind the body to equilibrate the fluid before outflow. The theoretical line in Figure 5.5 has a different slope from the one along which the measured points lie; this is due to the effects of the flow in the vicinity of sinker ends, which increase the drag and, consequently, affect the actual terminal velocity v_0^*. Note that the calculated dataset foreshows actual terminal velocity approximately $v_0^* \approx -0.11\ \mathrm{m}\cdot\mathrm{s}^{-1}$. Neither do the points in Figure 5.6 lie on the theoretical curve precisely, but the extent of the end effects is negligible.

5.5.2 Effect of the symmetry constraint

Figure 5.7 shows the the dependence of the force on the wall Γ_{-2} on the sinker velocity v^*. One can see that the Dirichlet set exhibits less variation due to the mesh refinement and thus can be considered more accurate.

5.5.3 Effect of the mesh refinement

The accuracy of the force obtained by integration of the stress tensor components apparently depends on the approximational properities of the discrete functional spaces.

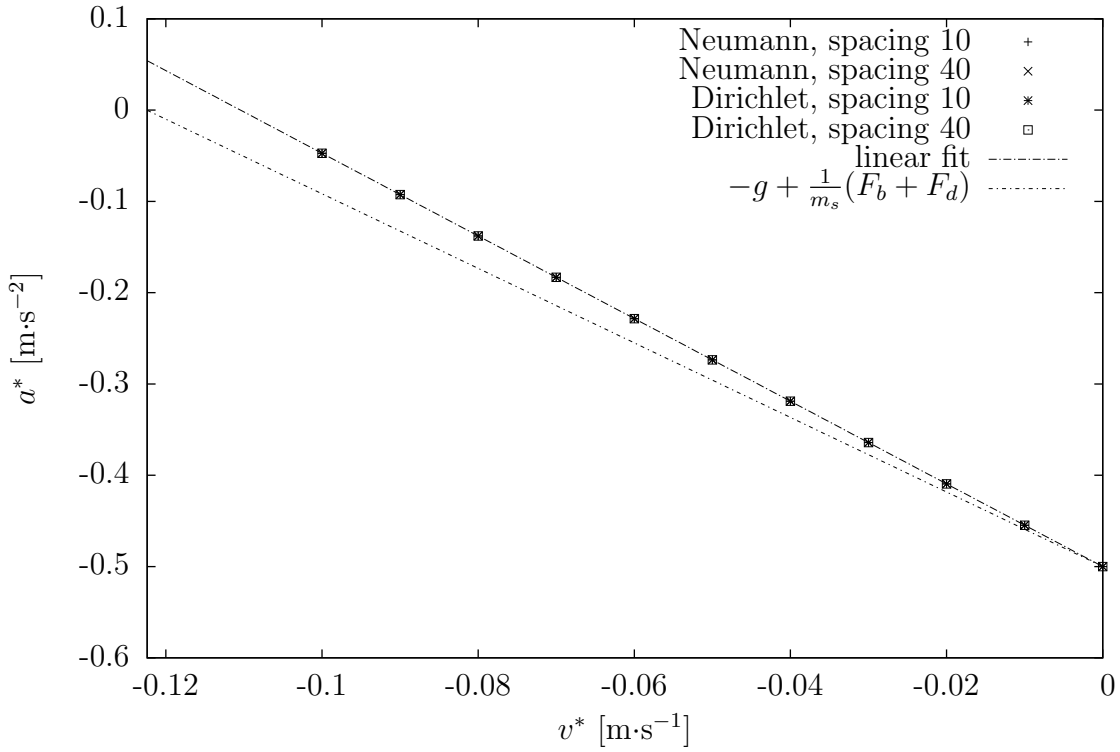

Figure 5.5: Total force on the sinker for different values of v^*. 2x regular mesh refinement.

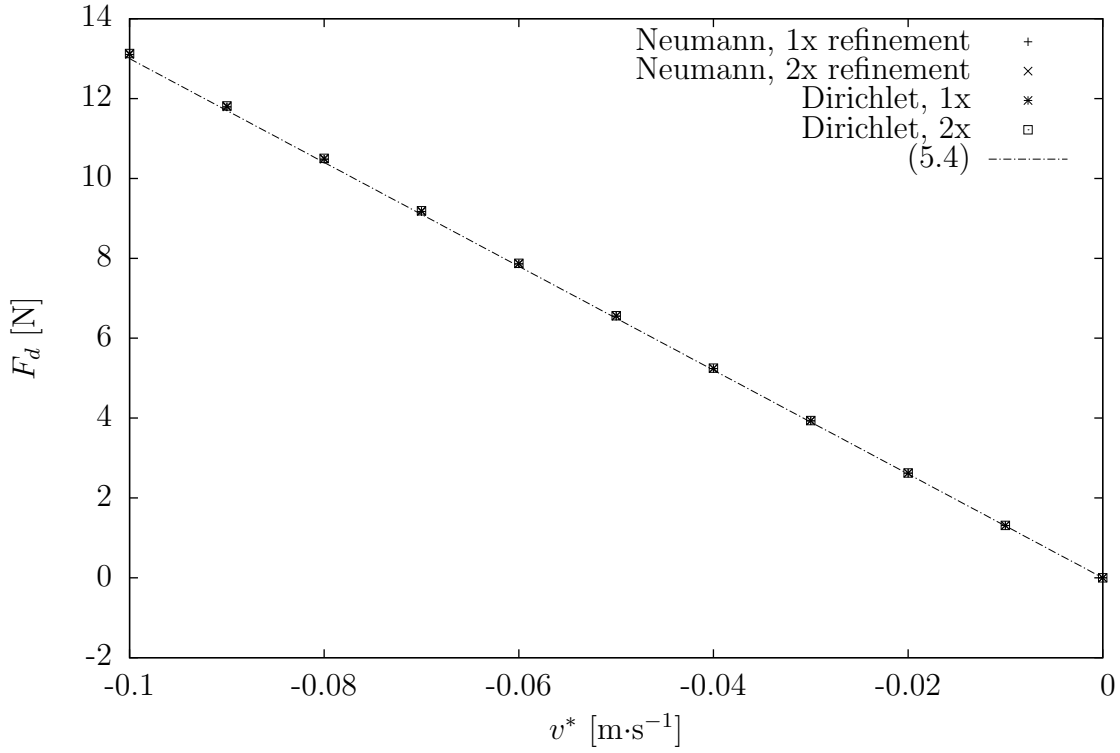

Figure 5.6: Force on the wall Γ_{-3} parallel to the tube walls.

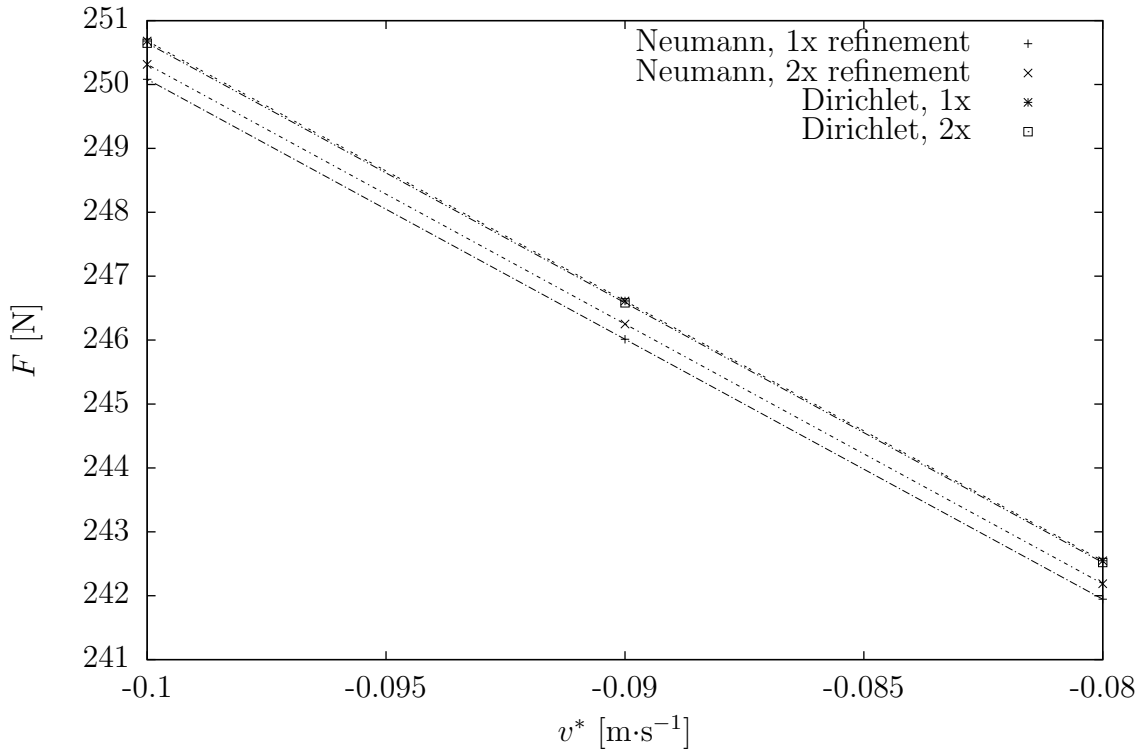

Figure 5.7: Force on the wall Γ_{-2} (the "leading edge").

In addition to *regular* mesh refinement $\mathcal{T}_{\frac{h}{2}}$ derived from $\mathcal{T}_h$ by dividing each quadrilateral into four, we also investigated an *adaptive* approach, refining elements pertaining to boundaries $\Gamma_{-2,-3,-4}$ only. The latter discretization is an example of a nonconforming method; the discrete approximations need not to be in the space where the solution of the continuous problem is sought. Figure 5.8 shows that the adaptive refinements do not behave in an uniform trend. The flow in the vicinity of the $\Gamma_{-2,-3,-4}$ boundaries may be significantly influenced from "poorly approximated" farther regions, so that the level of regular mesh refinement seems principal. However, in a more stringent geometry ($\frac{b}{\Sigma} \approx 10^{-2}$) such a discretization can considerably reduce compuational demands at keeping the accuracy acceptable.

5.6 The unsteady problem

The unsteady calculations presented below were done with the same set of parameters as the force calculations. We settled for the Dirichlet approach to ensure symmetry. The method for integrating the equation of motion was adapted to include a fixed-point iteration at each time step so as to increase the numerical stability. This led to a distinct variant of a predictor corrector method with damping; see Algorithm 2.

The damping parameter $\theta \equiv$ `th` was chosen empirically; the lower value of `th` reduced the force oscillations at the cost of more corrector iterations. The initial value for `th` was 0.1, `tol` was set at 10^{-2}. Likewise, the timestep `dt` needs to be

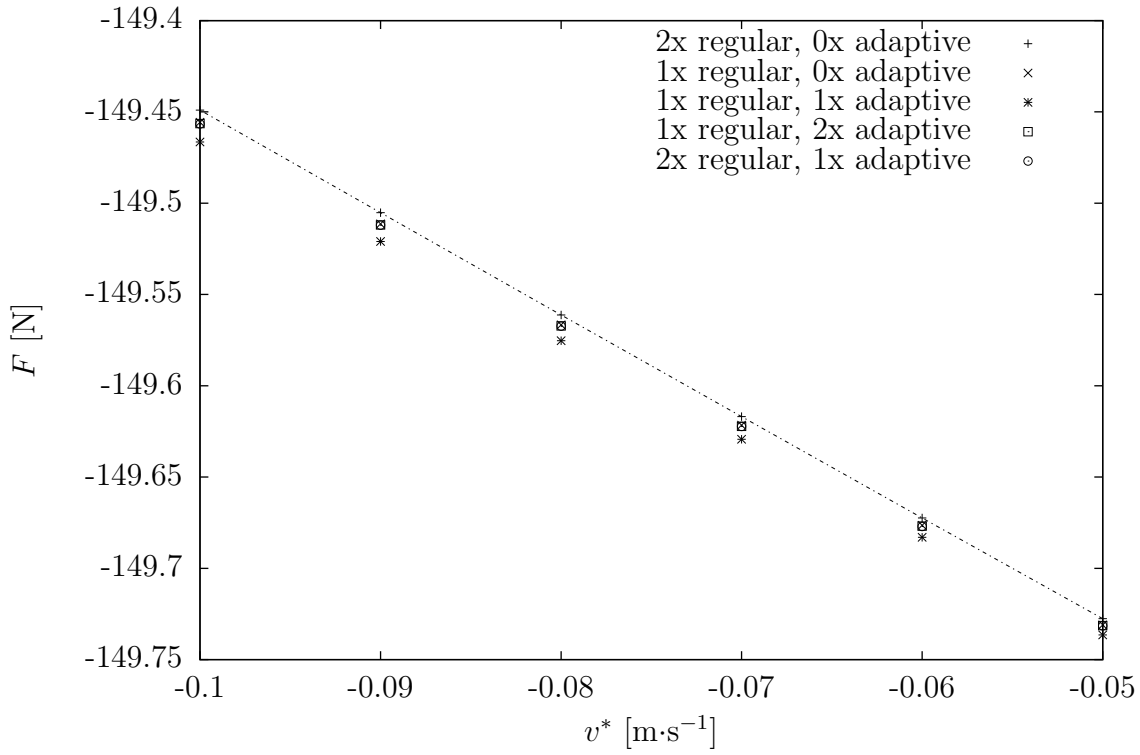

Figure 5.8: Force on the wall Γ_{-4} ("trailing edge") for different levels of adaptive refinement.

Σ	3	m
b	2	m
d	20	m
ρ_s	2	kg·m^{-2}
ρ_f	1	kg·m^{-2}
μ	1	Pa·s·m
g	1	m·s^{-2}

Table 5.1: Parameters for the unsteady 2D computations with Navier-Stokes fluid.

chosen small enough that

$$|v^*(t) + a^*(t)\Delta t| < v^*_{term} \tag{5.9}$$

holds during the body equilibration. Table 5.1 sums up the parameter values used for the unsteady calculation, unless stated otherwise.

Figures 5.9, 5.10 compare the solution $v^*(t)$, $a^*(t)$ obtained by means of the explicit Euler and damped predictor-corrector. The solution for force demonstrates the instability of the explicit Euler method. The predictor-corrector method was the method used in subsequent calculation foremost due to better behaviour as opposed to Euler method.

Figures 5.11–5.14 illustrate the effect of the chosen solver constants on the solution. It turns out that timestep has greater impact on the solution[4] than

[4]As a function of time; the terminal velocity is not affected by chosen timestep.

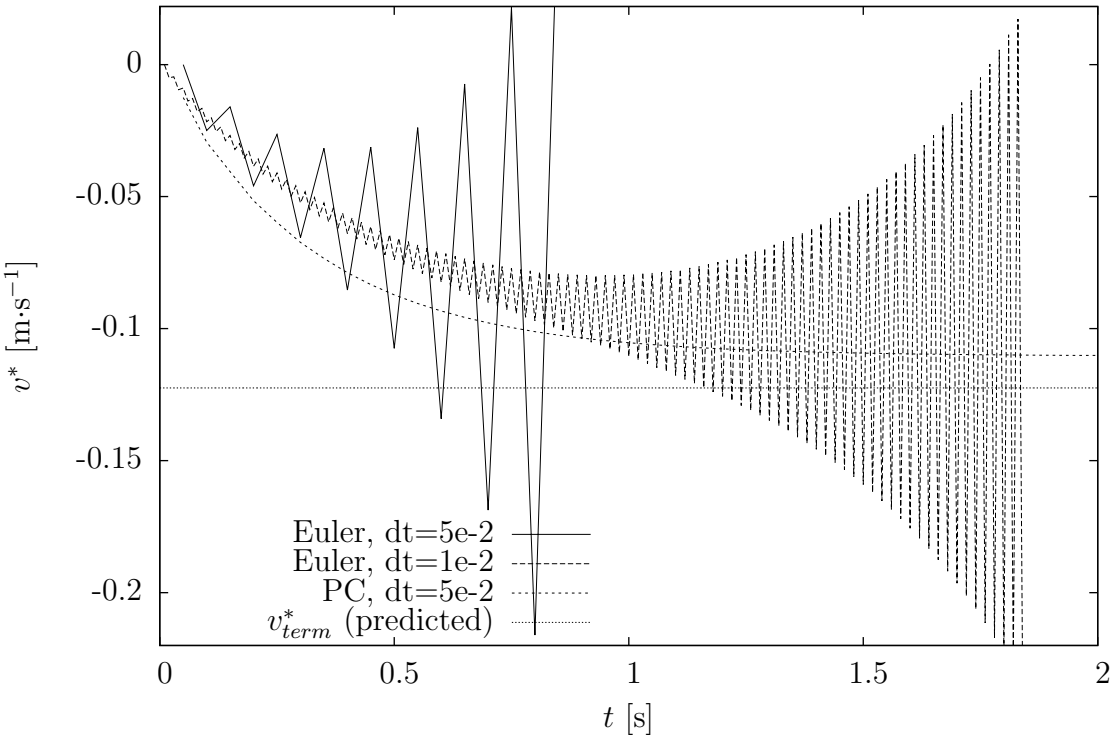

Figure 5.9: Time evolution of the sinker velocity.

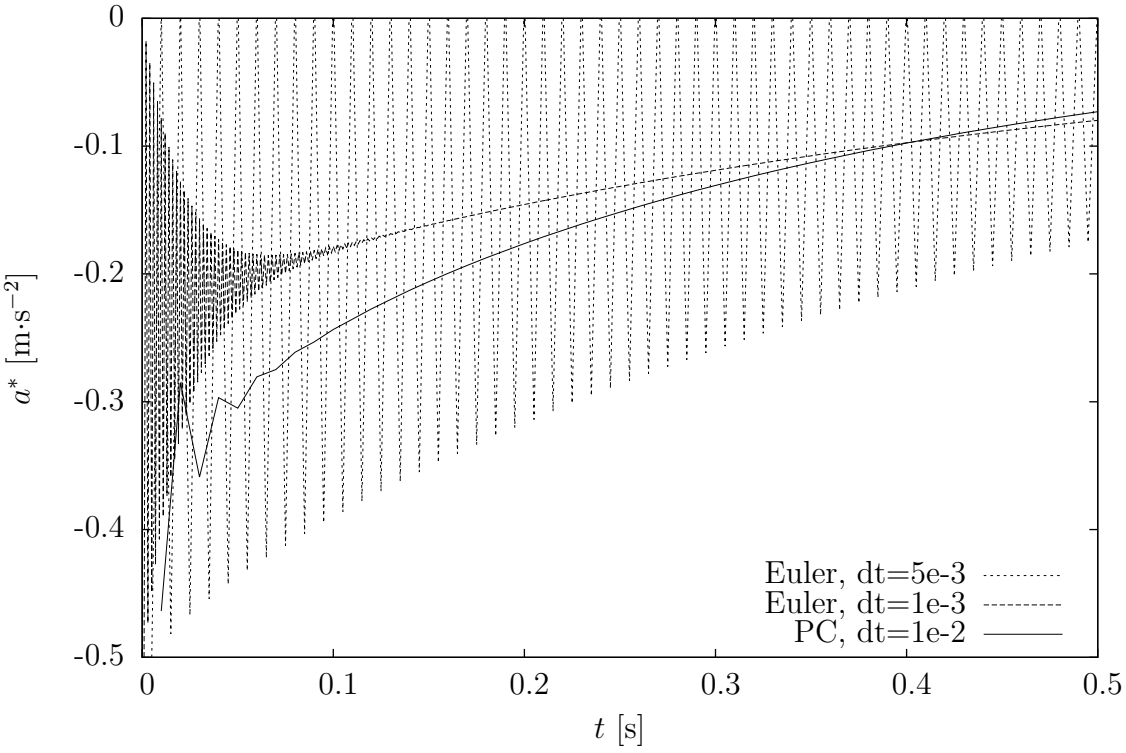

Figure 5.10: A comparison of sinker acceleration given by explicit Euler and damped predictor-corrector method.

Algorithm 2 The damped predictor-corrector method used for the euqation of motion of the body

$(z^*)^0 = 0$;
$(v^*)^0 = 0$
$(a^*)^0 = 10^{-10}$
while $|(a^*)^n| > 10^{-15}$ **do**
  solve NSE
  $F_d = \int_{\Gamma_{-2,-3,-4}} \mathbb{T}^n \mathbf{n} \, \mathrm{d}s$
  $(a^*)^{n+1} = -g + \frac{1}{m_s}[F_d]$
  $\widetilde{(v^*)} = (v^*)^n + (a^*)^{n+1}\Delta t$
  while $k < 20$ **or** $\frac{\widetilde{(a^*)} - (a^*)^n}{(a^*)^n} >$ `tol` **do**
    $\widetilde{(v^*)} = (v^*)^n + \frac{1}{2}\widetilde{(a^*)}\Delta t$
    $k = k + 1$
    solve NSE with $(v^*)^n$
    $F_d = \int_{\Gamma_{-2,-3,-4}} \mathbb{T}^n \mathbf{n} \, \mathrm{d}s$
    $\widetilde{(a^*)} = \theta(-g + \frac{1}{m_s}[F_d]) + (1-\theta)\widetilde{(a^*)}$
  end while
  $(a^*)^{n+1} = \widetilde{(a^*)}$
  $(v^*)^{n+1} = \widetilde{(v^*)}$
  $(z^*)^{n+1} = (z^*)^n + (v^*)^{n+1}\Delta t$
end while

the weight factor `th` in the predictor-corrector method. On the other hand, even negligible differences in the force can lead to a slightly shifted value of reached terminal velocity v_0^*. The terminal velocity predicted by (5.6) is not reached precisely due to end effects.

Figures 5.15 and 5.16 explain the analogy between the falling rectangle in an infinite channel and real FCV experimental setup: The former shows that the reciprocal of the terminal velocity (i.e. the time that takes the equilibrated sinker to fall a unit distance) is indeed proportional to viscosity. The latter explains the role of end effects: theoretical terminal velocity calculated for an inifinite rectangle (i. e. the falling plates) was based on the assumption that the end effects could be neglected. The end effects for the finite body are always present, but slowly decay as the sinker gets longer. The data in Figure 5.16 were fitted to a function $f(d) = v^*_{term} + \frac{\alpha_{FRV}}{d}$. It can be shown that α_{FRV} depends only on Σ and b. The dimensionless quantity $\frac{f(d)}{v^*_{term}} = 1 + \frac{\alpha_{FRV}}{v^*_{term} d} = ECF^{-1}$ is the reciprocal of the *end correction factor* given by the ratio of the predicted and actual terminal velocity:

$$ECF = \frac{v^*_{term}}{v^*_0}$$

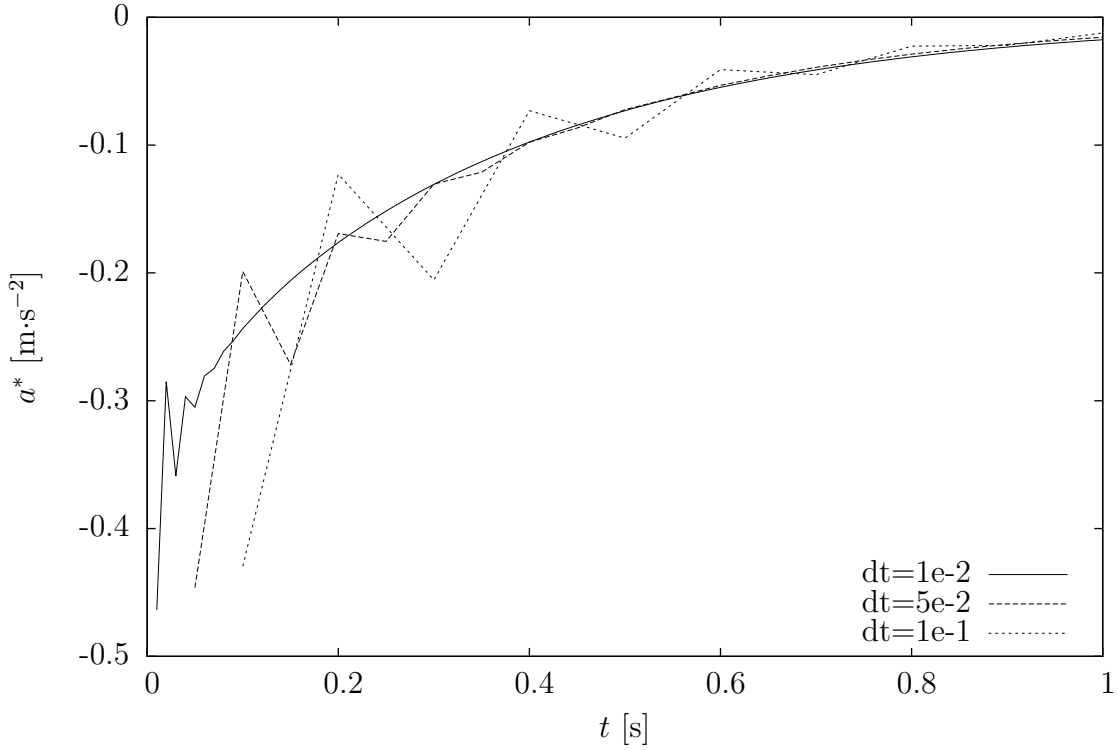

Figure 5.11: Sinker acceleration for different timesteps of damped predictor-corrector. Damping parameter `th` set to 0.25. Refer to Table 5.1 for parameter values.

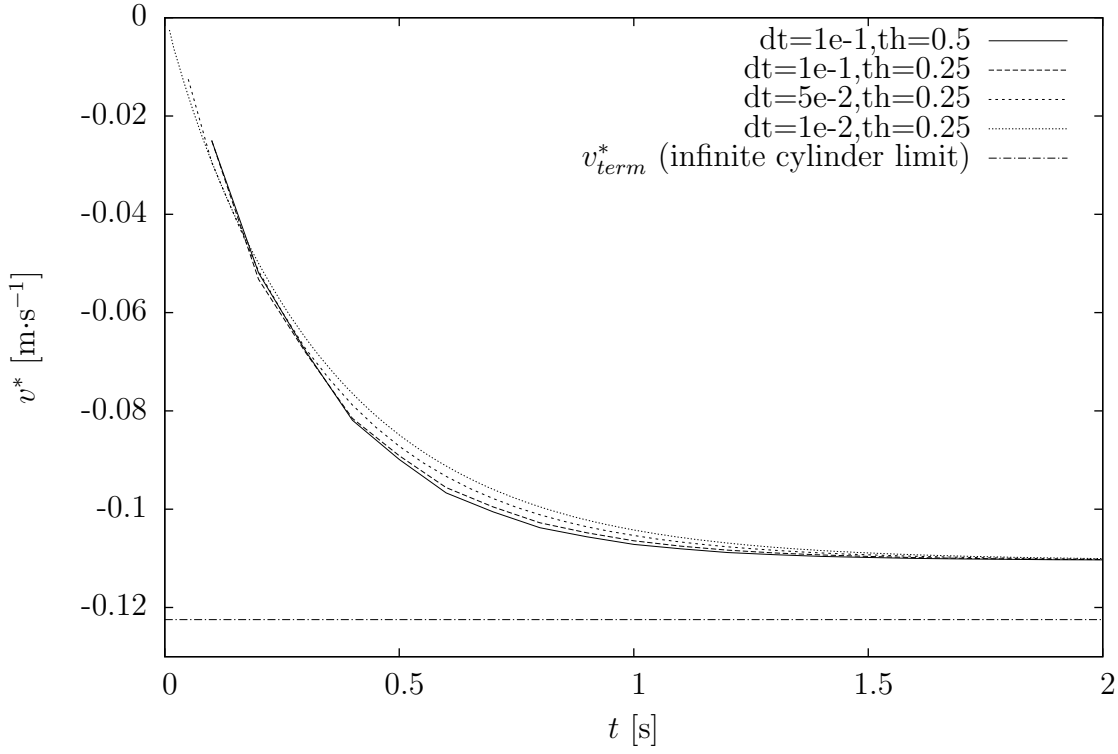

Figure 5.12: Sinker velocity for different timesteps of the predictor-corrector method. The value of v^*_{term} was calculated from (5.6).

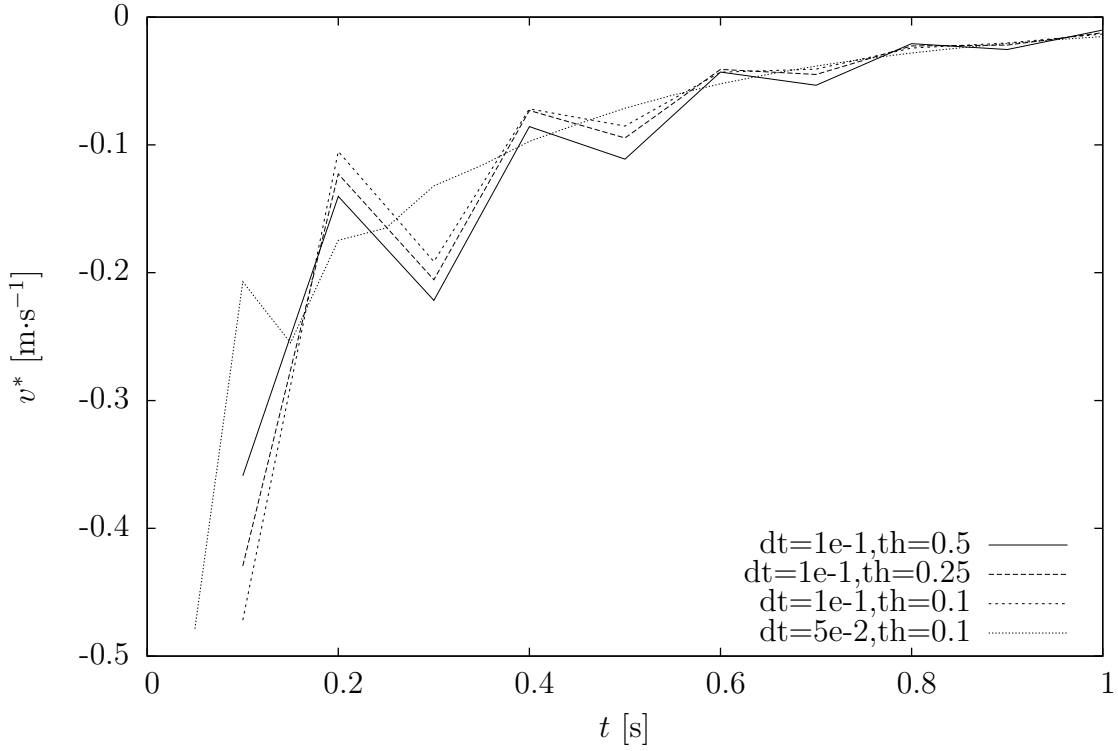

Figure 5.13: Sinker acceleration for two values of damping parameter `th`.

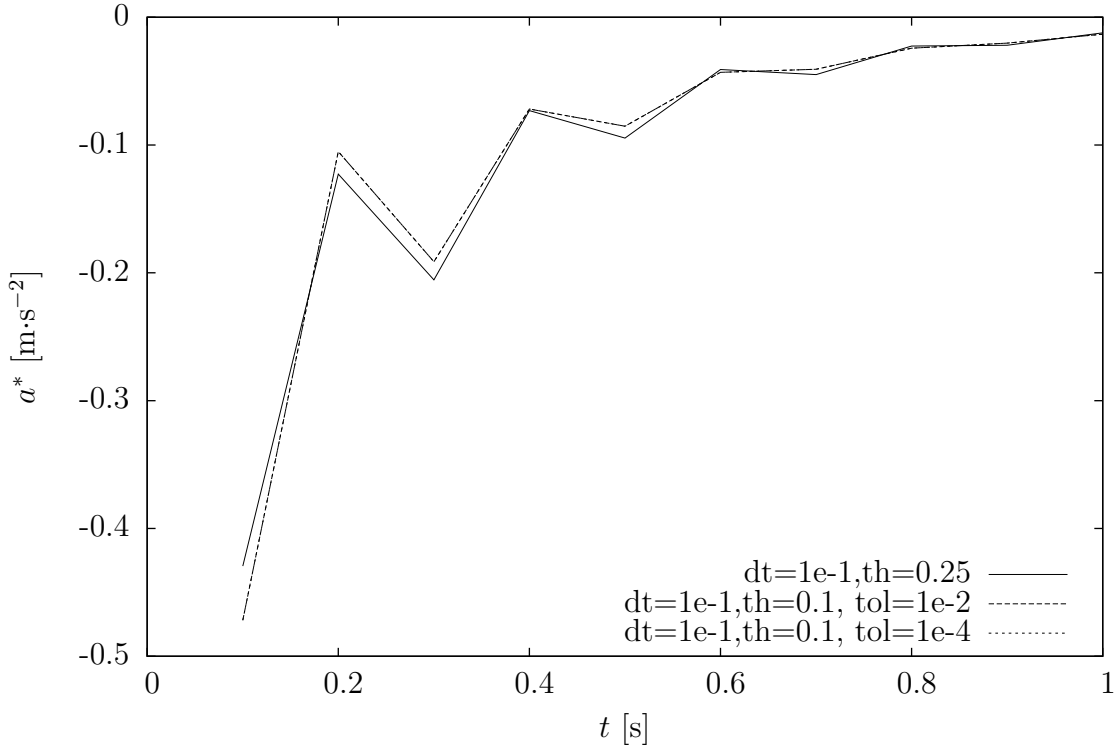

Figure 5.14: Sinker acceleration for two values of relative force tolerance.

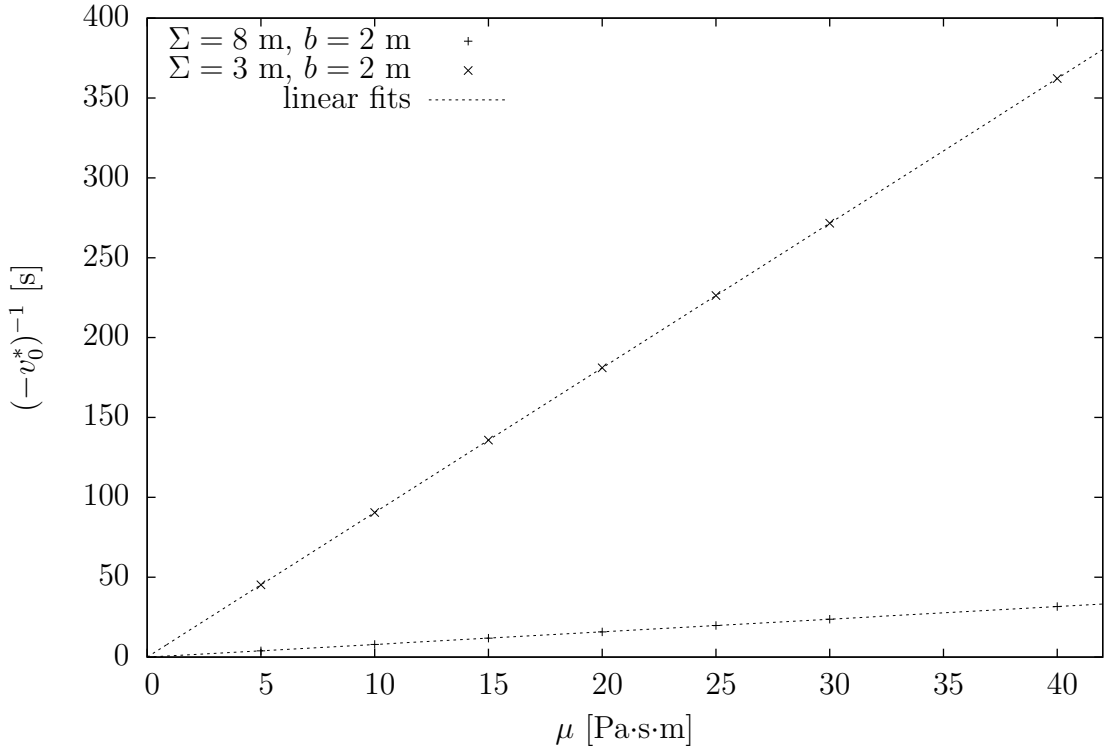

Figure 5.15: The linear dependence of terminal velocity reciprocal on the viscosity.

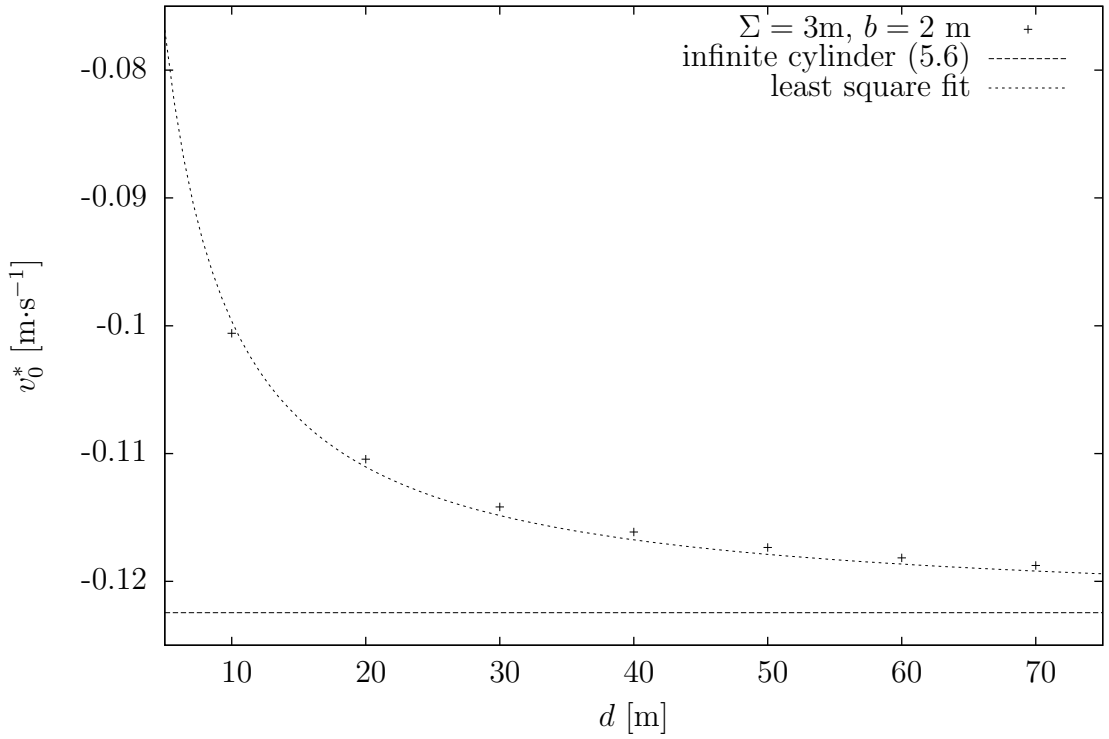

Figure 5.16: Terminal velocities for different sinker lengths.

6. Fall of a cylinder in an infinite tube

The numerical method for motion of a rectangle in an infinite channel can be easily extended to three spatial dimensions.

6.1 Flow equations

Unlike the case of the piezoviscous Poiseuille flow in a pipe, we were not able to use the original formulation of the momentum balance (4.6) directly as the division by r led to simulation crashes.

The equations used in the finite element code were formulated in terms of the equation residue as follows:

$$\Phi_{\boldsymbol{p}}(\mathbf{v};q) = \int \left(r\frac{\partial v^r}{\partial r} + r\frac{\partial v^z}{\partial z} + v^r \right) q \,\mathrm{d}r\,\mathrm{d}z,$$

$$\begin{aligned}\Phi_{\boldsymbol{v}^r}(\mathbf{v},p;\boldsymbol{\varphi}) = & \\ & \int \left[r^2\rho_f \left(v^r\frac{\partial v^r}{\partial r} + v^z\frac{\partial v^r}{\partial z} \right) - 2rp + 2\mu v^r \right] \varphi^r + \\ & + r^2 \left(-p + 2\mu\frac{\partial v^r}{\partial r} \right) \frac{\partial \varphi^r}{\partial r} + r^2\mu(p) \left(\frac{\partial v^r}{\partial z} + \frac{\partial v^z}{\partial r} \right) \frac{\partial \varphi^r}{\partial z} \,\mathrm{d}r\,\mathrm{d}z,\end{aligned}$$

$$\begin{aligned}\Phi_{\boldsymbol{v}^z}(\mathbf{v},p;\boldsymbol{\varphi}) = & \\ & \int \left[r^2\rho_f \left(v^r\frac{\partial v^z}{\partial r} + v^z\frac{\partial v^z}{\partial z} \right) + g + \frac{\mathrm{d}v^*}{\mathrm{d}t} \right] \varphi^z + \\ & + \left[\mu r \left(\frac{\partial v^r}{\partial z} + \frac{\partial v^z}{\partial r} \right) + r^2\mu \left(\frac{\partial v^r}{\partial z} + \frac{\partial v^z}{\partial r} \right) \right] \frac{\partial \varphi^z}{\partial r} + \\ & + r^2 \left(-p + 2\mu\frac{\partial v^z}{\partial z} \right) \frac{\partial \varphi^z}{\partial z} \,\mathrm{d}r\,\mathrm{d}z,\end{aligned}$$

6.2 Computational details

The discretization of the flow equations was done in the same manner as in the case of falling rectangle. In order to approximate real geometries with reasonable computational demands, the elements in the sinker-tube gap and in the vicinity of the sinker ends were made small, while the elements sufficiently distant can be as large as possible. The mesh generator takes into account the aspect ratio for the quadrilateral elements $\lesssim 8$. An exaple of resulting mesh is given in Fig. 6.1. For larger gaps the mesh from 2D simulations was used; both kinds of computational meshes inherited the boundary notation from the planar case.

Let us briefly remind the boundary conditions. The Dirichlet condition $\mathbf{v} = -v^*\mathbf{e}_z$ was prescribed at boundaries $\Gamma_{-7,-8}$ and $\mathbf{v} = \mathbf{0}$ at $\Gamma_{-2,-3,-4}$. The symmetry conditons $v^r = 0$, $\frac{\partial v^z}{\partial r} = 0$ were prescribed at $\Gamma_{-1,-5}$ in the sense of Dirichlet condition. The outflow boundary Γ_{-6} was equipped with the stress condition

$$\mathbb{T}\mathbf{n} = (p_{conf} - \rho_f g z^*)\mathbf{n},$$

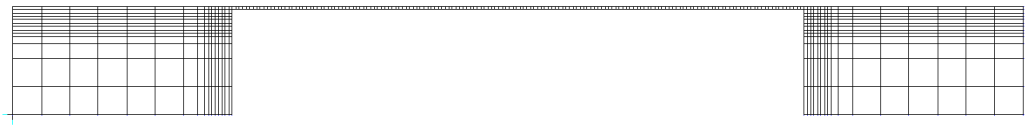

Figure 6.1: A snapshot of the optimized initial mesh. $R_1 = 3.84$ mm, $R_2 = 3.97$ mm, $L = 20.92$ mm. The dimensions taken from [30].

accounting for the increase of the hydrostatic pressure at the top of the sinker as it gets deeper in the fluid.

The sinker equation of motion was solved using predictor-corrector method with damping described in the previous chapter. The damping parameter `th` was chosen empirically.

6.3 The effect of mesh refinement

The accuracy of the force exerted by the flow past the cylinder may substantially influence the value of the terminal force. To determine the magnitude of such effects, we performed a series of calculations with fixed material and geometrical parameters for first three levels of adaptive and global mesh refinement. The *adaptive* refinement concerned the sinker bases and walls; elements lying at the boundaries $\Gamma_{-2,-3,-4}$ were refined. Such a numerical experiment also helped to assess the uncertainity level of subsequent calculations. Table 6.1 sums up the results for two artificial[1] sets of geometrical and material parameters. The Reynolds number was approximated, using theoretical v^*_{term} as the characteristic velocity, as follows [9]:

$$Re = \frac{2R_1^2 v^*_{term} \rho_f}{\mu_0 (R_2 - R_1)} \tag{6.1}$$

Calculation adressed further were performed with successively one and two regular mesh refinements. The difference of the settling velocity served as an empirical error estimate.

6.4 The effect of the sinker ends

When performing an experiment with falling cylinder viscometer, the terminal velocity attained is somewhat less than predicted by theory.

One approach is to measure the *relative* viscosity and calibrate the viscometer via determining the terminal velocity for a fall in a liquid with known viscosity. This method was adopted by Bridgman. The other option is to assume that the actual terminal velocity is diminished by a correction factor ECF close to unity, dependent on the geometrical parameters of the viscometer only.

The effect of the flow near the sinker bases was studied theoretically by Park and Irvine [32]. They considered the drag of a rigid disk in the Stokes flow and

[1]The FCV dimensions used in Table 6.1 do not represent any particular setup used in experiments, although they are based on real geometries [6], [16] in terms of the order of magnitude of the measures.

ref. level		Adaptive		
Global		0	1	2
0	**A**	-4.459873e-04	-4.460508e-04	-4.460508e-04
1		-4.460851e-04	-4.461336e-04	-4.461749e-04
0	**B**	-3.836718e-05	-3.836729e-05	-3.836798e-05
1		-3.836791e-05	-3.836857e-05	-

	parameters
A	R_1=4.75 mm, R_2 =5 mm, h = 52.2 mm ρ_s =7867 kg·m^{-3},ρ_f =2400 kg·m^{-3} g =10 m·s^{-2} μ =0.718 Pa·s; v^*_{term}=-3.859773e-05 m·s^{-1}, $Re \approx 0.023$
B	R_1=4.5 mm, R_2 =5 mm, h=18 mm ρ_s =7867 kg·m^{-3} ,ρ_f =2000 kg·m^{-3} g =10 m·s^{-2}, μ =0.5 Pa·s; v^*_{term} =-4.611129e-04 m·s^{-1}, $Re \approx 0.15$

Table 6.1: Comparison of calculated terminal veloctites for various mesh refinement levels. `th`=0.25, `dt`=1e-4.

superimposed the force with the drag on the cylinder walls. Their expression for the correction factor is, setting $k = \frac{R_1}{R_2}$,

$$ECF = 1 + \frac{8}{\pi}\frac{k}{C_w}\left(\frac{k^2(1-\ln k)-(1+\ln k)}{h(1+k^2)}\right),$$

where the wall correction factor C_w for a disc is given by

$$C_w(k) = 1.003852 - 1.961019k + 0.9570952k^2.$$

An empirical formula for the end correction factor was derived by Wehbeh and Ui [33]. Introducing a dimensionless parameter $x = \frac{R_2-R_1}{h}\sqrt{\frac{R_1}{R_2}}$, one can approximate the end correction factor by

$$ECF = 1 + (1.67x - 0.017).$$

To check the liability of our numerical results, we computed[2] the "numerical" terminal velocity v_0^* for different levels of mesh refinement and values of material parameters (ρ_f, ρ_s, μ.) Table 6.2 shows the $ECF = \frac{v^*_{term}}{v_0^*}$ for various geometries. While the formula for ECF was derived analytically in [32], Wehbeh and Ui used the experimental data for rather short cylinders. As noted in [32], their formula fails for long cylinders in narrow gaps, predicting ECF lower than 1, clearly an unphysical value.

Figure 6.2 shows end correction factors in dependence on the tube radius R_2. The larger errorbars in the region of higher values of $\frac{R_2}{R_1} \geq 1.11$ are due to different mesh partitioning used. The ECF value is clearly approaching 1 as $R_2 \to R_1$, though at a slightly different slope in comparison to the theoretical values as of

[2]The numerical results presented in this section were obtained using the resources of MetaCentrum National Grid Infrastructure and CERIT-SC clusters. All other computations were carried out on the Sněhurka cluster.

	R_1	R_2	h	$\frac{R_1}{R_2}$	x [33]	ECF (num.)	ECF [33]	ECF [32]
	8	10	50	0.8	0.03578	**1.044**±0.002	1.0427±0.0038	1.0311
	4.5	5	18	0.9	0.02635	**1.034**±0.002	1.027 ±0.0069	1.0174
[31]	3.71	3.892	10.55	0.953	0.01684	**1.015**±0.007	1.0111±0.0082	1.0078
	18	20	150	0.9	0.01265	**1.016**±0.006	1.0041±0.0013	1.0084
	4.75	5	52.2	0.95	0.00467	**1.006**±0.002	0.9907±0.0022	1.0022
[30]	3.84	3.97	20.92	0.967	0.00611	**1.008**±0.001	0.9932±0.0029	1.0022

Table 6.2: End correction factors computed for a fall of a cylinder in an infinite closed tube.

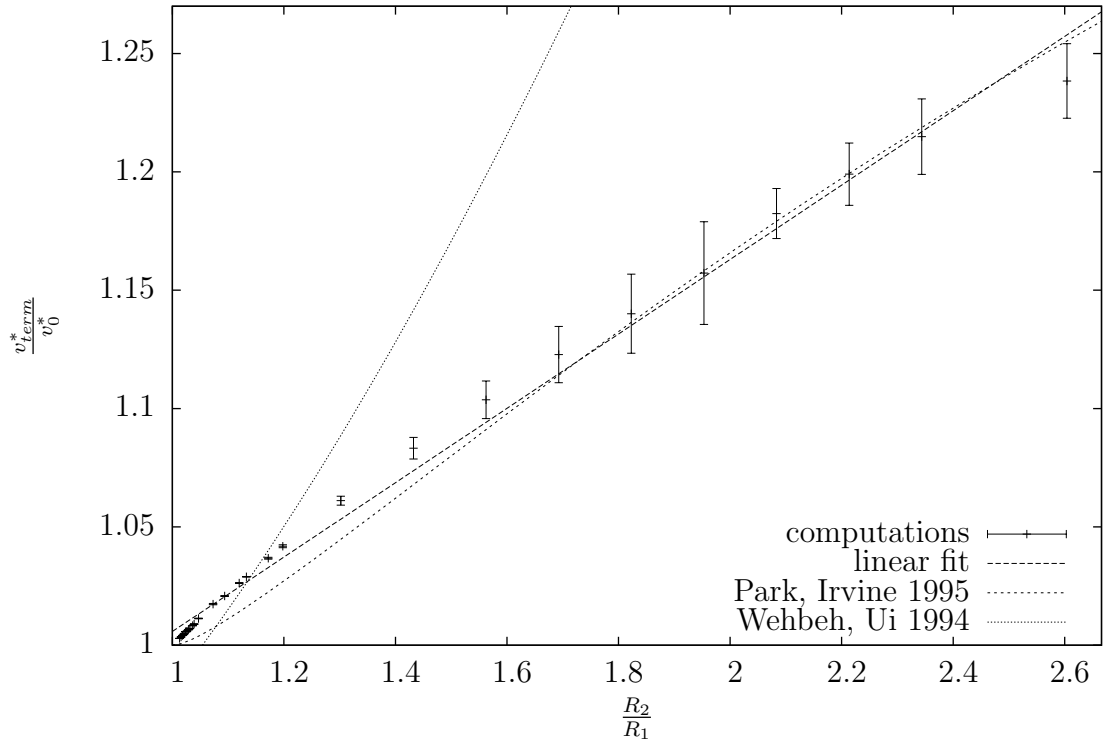

Figure 6.2: End correction factors for varied R_2. $R_1 = 3.842$ mm, $h = 20.92$ mm, $\rho_s = 7874$ kg $\cdot$ m^{-3}, glycerol-filled.

[32]. Nevertheless, the computed ECF is matched well to the theoretical values as far as wide gaps are concerned. Similarly to Table 6.2, the accordance with [33] is achieved in a very narrow region around $\frac{R_1}{R_2} \approx 1.15$.

Figure 6.3 depicts the end correction factors for different sinker lengths considered. At high values of h (i. e. the sinker being virtually infinite) the end effects are almost negligible and the computed points are very close to the theoretical predictions of Park and Irvine. On the other hand, in the short ("the circular disc") limit, the theoretical predicion is substantially different from the numerical observations. The main reason lies in the fact that the wall correction factor C_w as used by Park and Irvine was obtained from incomplete data, lacking correct values for $k \approx 1$, the case in the present study; the empirical predictions of Wehbeh and Ui are much closer to calculated data in this particular case.

Figure 6.4 depicts the dependence of the viscous drag on the tube radius. The remaining geometrical and material parameters were the same as in the previous

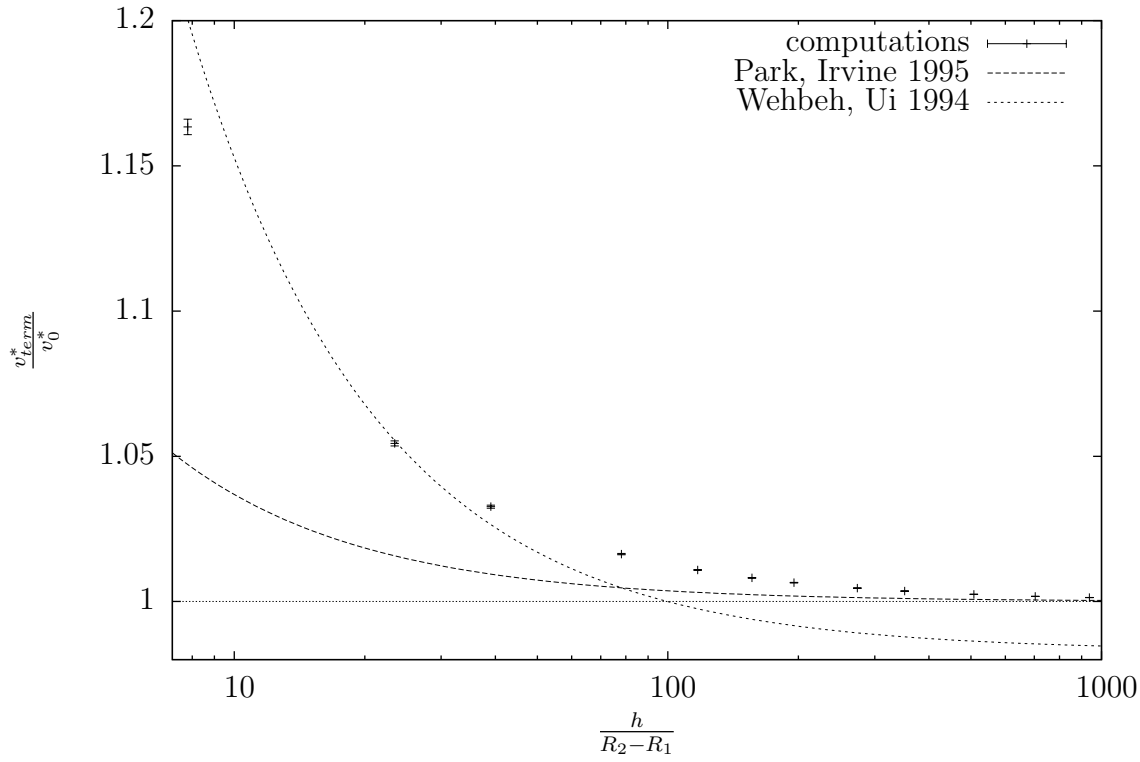

Figure 6.3: Dependence of the end correction factor on sinker length h. $R_1 = 3.842$ mm, $R_2 = 3.97$ mm.

figures. The drag rapidly decreases with increasing R_2. Firstly, (2.1) implies that the fluid velocity in the vicinity of the sinker lateral walls decreases and, secondly, the velocity gradient is smaller as the variation of the velocity takes place in a broader region. At $\frac{R_2}{R_1} = 5.2$ we see a significant departure from the theoretical curve; the flow at the ends is dominating the viscous drag.

The dependence of the buoyancy on R_2 is given in Figure 6.5. The buoyancy also decreases when R_2 is increased; when R_2 is small, the buoyancy is dominated by the "dynamic" contribution (2.4) due to high value of U (2.3). Considering the asymptotic behaviour for large R_2, we see that F_d reduces to the static buoyancy by virtue of the Archimedes law. Note that equation (2.3) implies that $U \to 0$ when $R_2 \to \infty$.

Figure 6.6 views the total force on the sinker for the sinker motion at the terminal velocity calculated for each tube size from (2.6). Hence, theoretical total force by (2.4,2.5) corresponds to $F_{tot} = 0$ in the figure. In accordance with Figure 6.2, the force for large tubes is greater, meaning that ratio between the predicted terminal velocity and the actual settling velocity will be greater. On the other hand, the actual force for narrow gaps is rather small, meaning that the predicted terminal velocity is matched closely.

For very large tubes the flow changes its nature and the equation (2.6) cannot be used to predict the terminal velocity of the sinker.

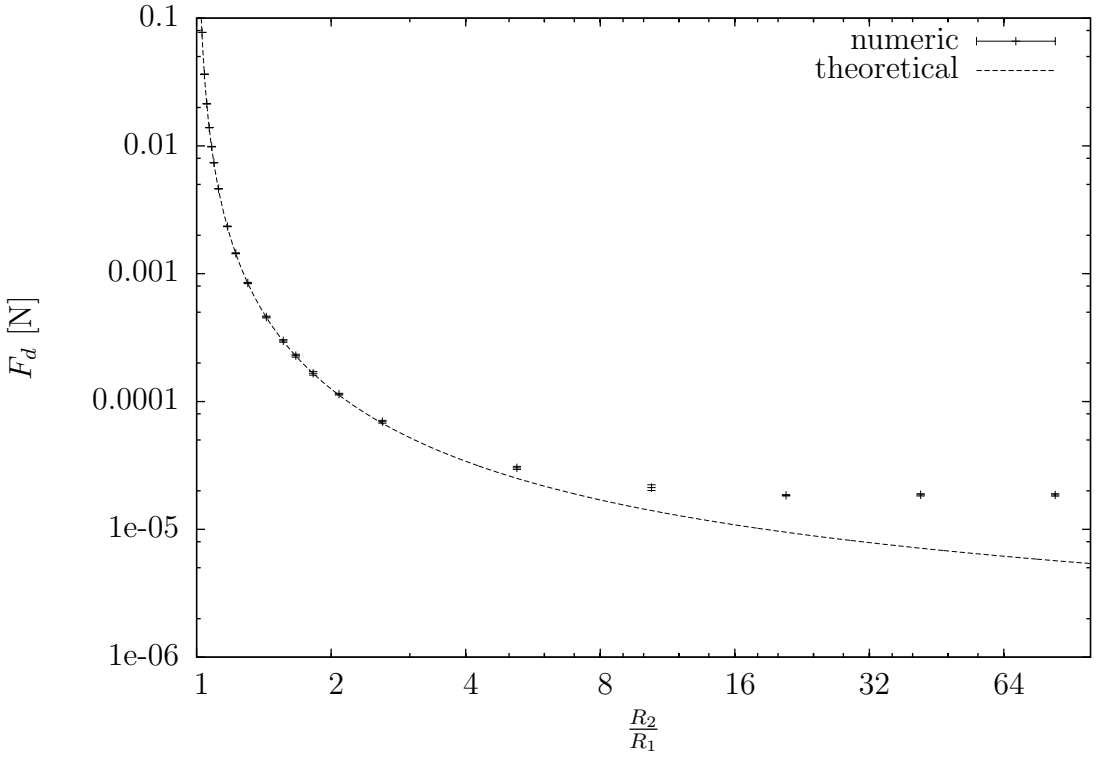

Figure 6.4: Viscous drag for different values of R_2.

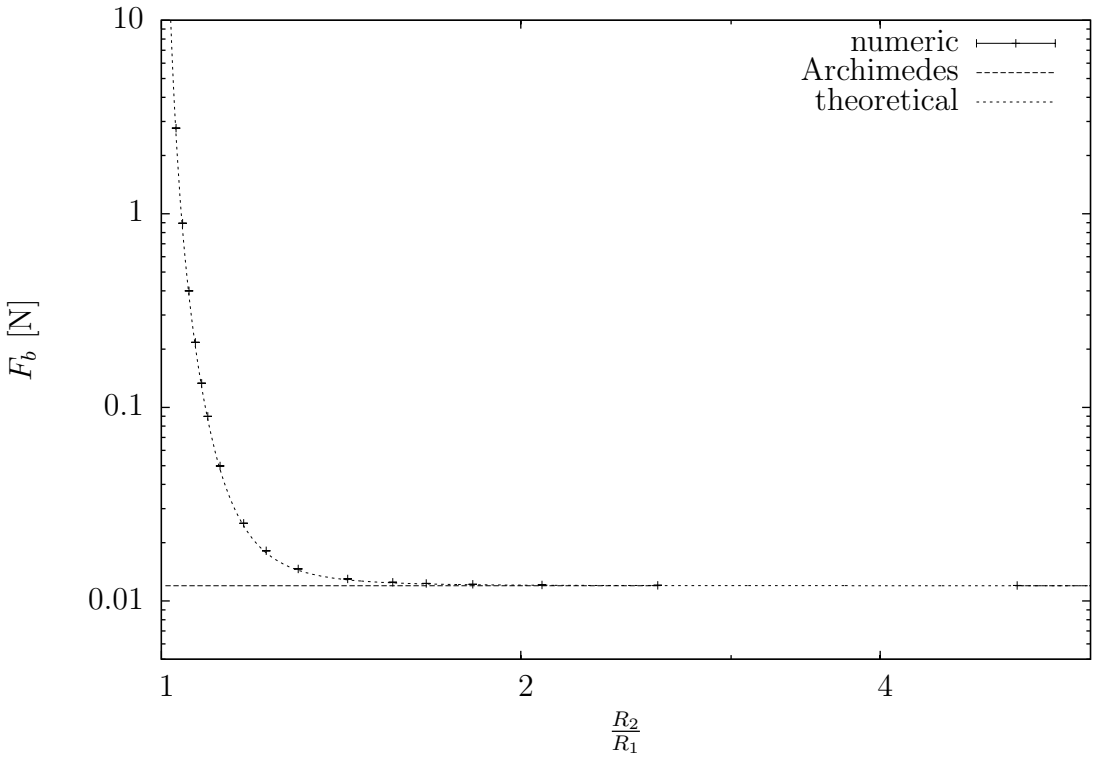

Figure 6.5: The buoyancy for different values of R_2.

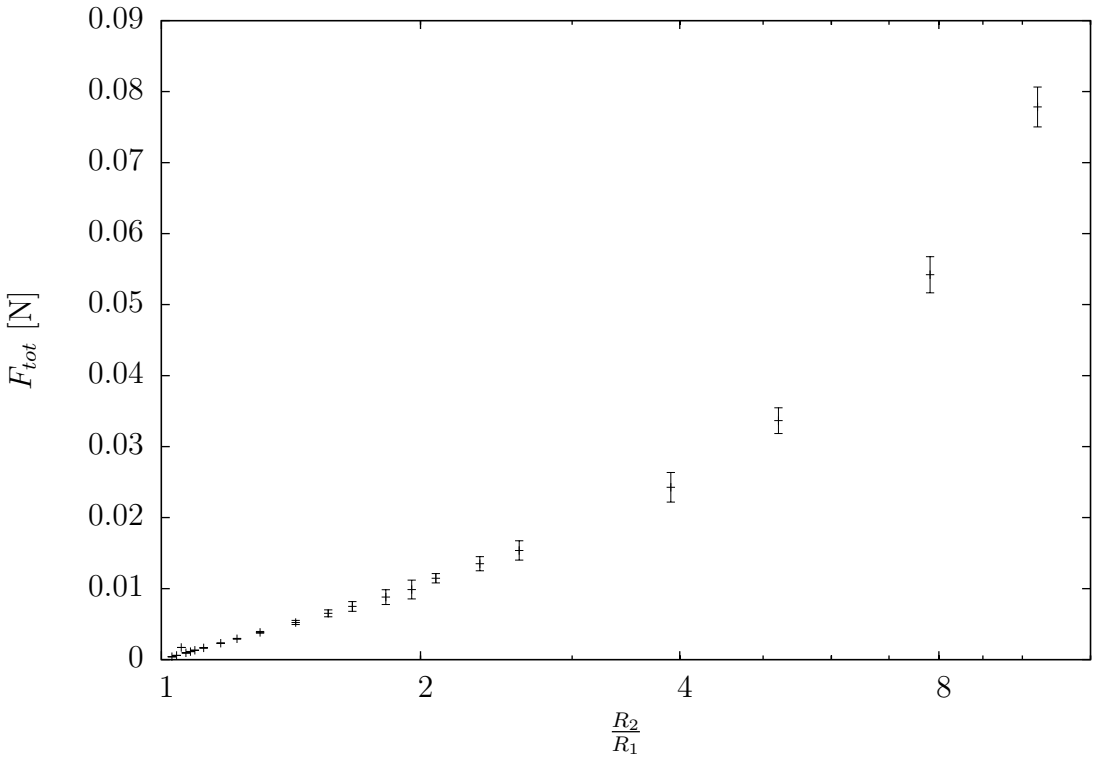

Figure 6.6: Total force on the sinker for different tube radii at corresponding terminal velocities.

6.5 Fall in a piezoviscous liquid

The main goal of the thesis was to perform a numerical simulation of a body falling in a piezoviscous fluid with constitutive relation

$$\mu(p) = \mu_0 \exp(\beta p).$$

In order to get observable results, we were led to choose a sufficiently dense fluid. The fluid should be also viscous enough to maintain the finite element solution tractable. It turned out that concentrated sulphuric acid with $\rho_f = 1261\ \mathrm{kg \cdot m^{-3}}$ and $\mu_0 = 1.48\ \mathrm{Pa \cdot s}$ fitted these considerations reasonably. The density of iron $\rho_s = 7874\ \mathrm{kg \cdot m^{-3}}$ was chosen for the sinker, length of the sinker h was 20 mm.

Since the piezoviscous effect were rather small, we increased the gap size by choosing $R_1 = 3$ mm, R_2=5 mm, thus creating an enviroment suitable for reaching large sinker velocities (v^*_{term} predicted by (2.6) is 0.4 $\mathrm{m{\cdot}s^{-1}}$.) The terminal velocity in real geometries is three to four orders smaller; such a simulation would take months to finish considering the method developed so far. The Reynolds number for the described setup under the assumption of constant viscosity is 3.1. The largest value of β for a stable solution of equation of motion was found at $10^{-3}\ \mathrm{Pa^{-1}}$, considering $p_{conf} = 1$ kPa. As in the Newtonian case, the sinker was released from rest. Timestep was `dt`=0.01 s and weight parameter `th` was chosen at 0.1.

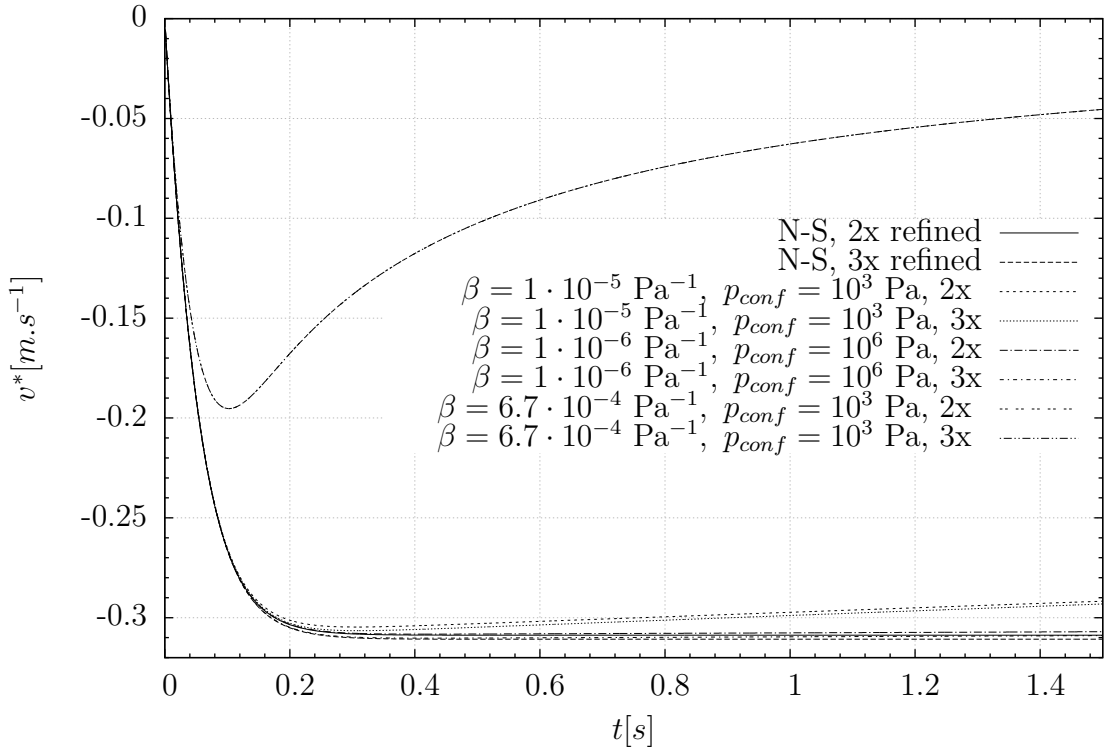

Figure 6.7: Evolution of the sinker velocity for different pressure-viscosity coefficients. The curves for $\beta = 6.7 \cdot 10^{-4}$ Pa^{-1} overlap.

Results

Figure 6.7 displays the sinker velocity v^* over time for different piezoviscosity coefficients β. We see that the least value of pressure-viscosity coefficient β considered (10^{-7} Pa^{-1}) differs from the solution for a Newtonian viscosity on the order of the N-S error, although the line for $\beta = 10^{-7}$ Pa^{-1} is still distinguishable. The measurements report values of β on the order 10^{-7} to 10^{-9} Pa^{-1} for real liquids. The values considered here are therefore somewhat exaggerated. Nevertheless, the curve for $\beta = 6.7 \cdot 10^{-4}$ Pa^{-1} illustrates qualitatively the piezoviscous effects. The sinker rapidly accelerates as though in Newtonian fluid, achieving soon a maximal speed of ≈ 0.2 m$\cdot$s^{-1}. Immediately the sinker starts to decelerate, meaning that the terminal velocity is not attained.

Figure 6.8 views the sinker position over time for different piezoviscosity coefficients β. The line for $\beta = 10^{-7}$ Pa^{-1} cannot be told apart from the Newtonian any more; this means that the time difference between the two cases is negligible (with respect to the error of the performed calculation,) although a hypothetical high precision velocity measurement based e. g. on a Doppler phenomenon [16] could tell the differece between the two cases. The line for $\beta = 10^{-6}$ Pa^{-1} gives a difference of about 0.015 s on 30 cm; this is on the order of the accuracy of time measurement [7]. Should (2.6) be used to determine the reference viscosity μ, the value would be overestimated by about 1.5%.

The viscometer tubes are actually made much shorter as they have to withstand large pressures. Even though, the piezoviscous effects are still present and can emerge when dealing with high-density liquids [2].

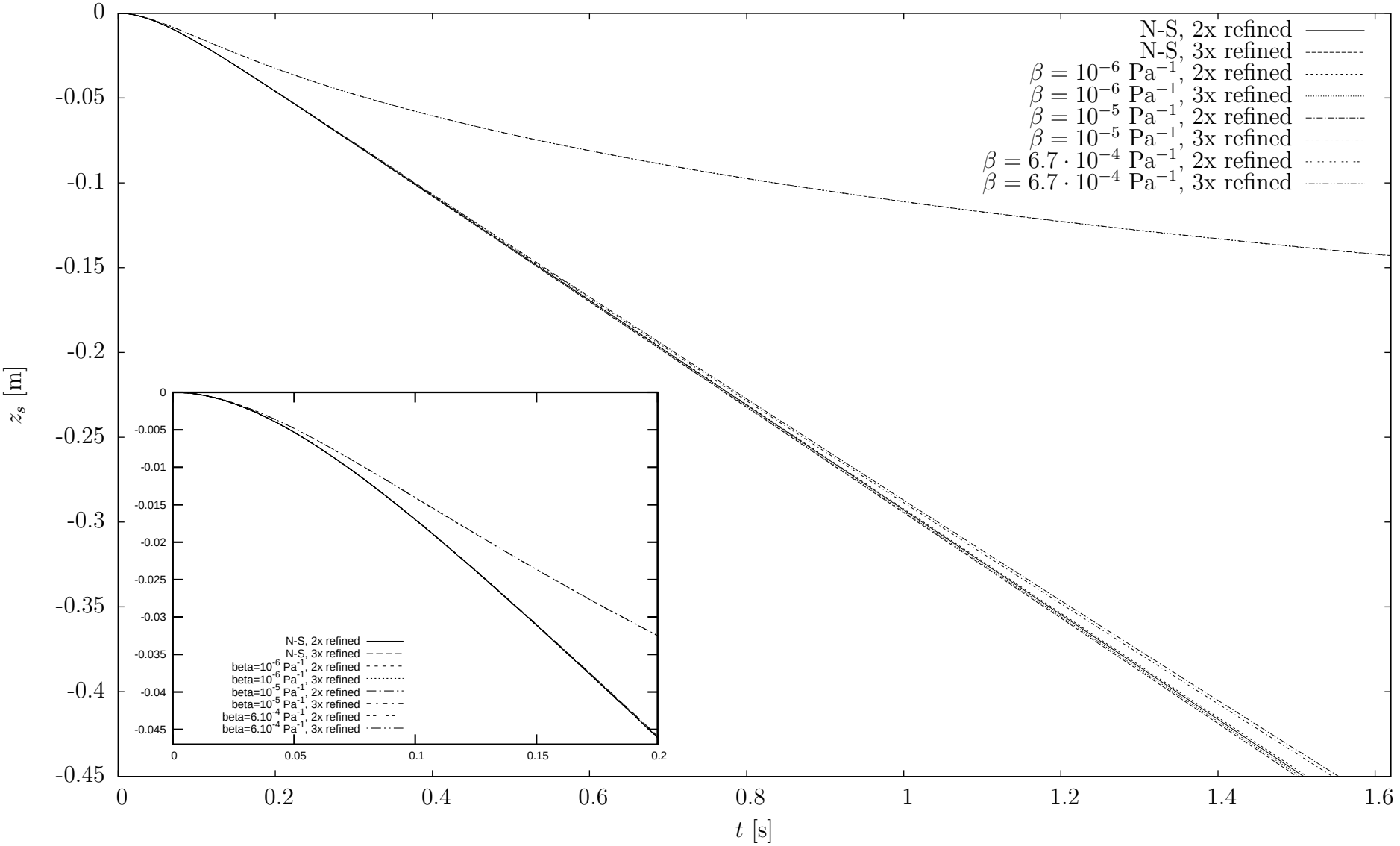

Figure 6.8: Position of the sinker over time.

Perspectives

Concerning the main goal of the thesis – a simulation of the FCV experiment with real data – the most significant limitation is the computational accuracy. If the simulations were carried out with narrower mesh and at greater refinement level, the fidelity of the results would hopefully permit us to consider values of β much closer to experimentally measured values, such as $5 \cdot 10^{-8}$ Pa^{-1} for toluene [7]. Furthermore, making use of more realistic material parameters would allow us to impose confining pressure of 10^7–10^8 Pa and get much closer to real experimental conditions [1],[7].

However, suggested change of the discretisation would lead to substantial increase in computational demands aside from shorter timesteps necessary due to lower terminal velocities in virtue of (5.9). Clearly, such a task cannot be done without some improvements to the computational method; for instance, since the matrix inversion takes most of the time in each Newton iteration, a different linear solver could be considered. Iterative methods such as *GMRES* [34] seem to be an attractive alternative to the present choice, taking into account that the problem of the body motion is in principle unsteady and that we are primarily interested in the quasi-equilibrium regime after the transient period due to release of the sinker. Moreover, iterative solvers can handle very large linear problems.Another option is to consider direct solver packages capable of parallel computations, for instance *SuperLU* [35].

The infinite channel approach discussed in the fall of a cylinder is somewhat unrealistic, although the computational method is not capable of longer simulations and we limit the distance travelled to a certain value in the simulations. In order to bring the FCV simulation to a more realistic setup, a numerical method for direct treatment of the body motion needs to be introduced. The *fictious domain* approach as of Glowinski *et al.* [36] appears suitable, since the the computational domain remains fixed and the body motion can be coupled to the flow problem more easily.

A prominent topic in the thesis assingment was to study the behaviour of the pressure in the vicinity of edges, as the fluid with pressure-dependent viscosity is expected to exhibit a significant departure form the Newtonian case. A theoretical study would necessarily include a perturbation analysis of the flow of a piezoviscous fluid past a nonocnvex corner; for analytical solution for the Newtonian fluid see [37]. A detailed numerical investigation of the pressure asymptotics needs to be carried out as well, since the situation in the viscometer is far more complicated compared to the case of a corner. The geometry considered in both the two- and three-dimensional case did not indicate singularities in pressure in the finite element solution, but, considering again the accuracy of the numerical solutions, the topic calls for a deeper investigation.

Conclusion

The topic of the present thesis was the motion of a body in an incompressible piezoviscous fluid in a special geometry of the falling cylinder viscometer. The work focused on performing the numerical simulations; in particular, we attempted to mimic real experimental conditions, assuming an incompressible fluid with pressure-viscosity relation

$$\mu(p) = \mu_0 \exp[\beta(p - p_0)].$$

Stating the problem, we were able to derive a semi-analytical formula for the settling velocity in a Newtonian fluid. Then, introducing a discretisation via the finite element method, we checked the order of the FEM approximation on simple flows of piezoviscous fluids with analytical solutions. A two-dimensional analogue of the fall problem was presented and numerically solved for the case of a Newtonian fluid in the reference frame attached to the body, discussing boundary conditions for the flow equations as well as the integration of the body equation of motion.

The results were then extended to the 3D case with cylindrical symmetry. A numerical study of the end effects for the falling cylinder viscometer was carried out, finding overall agreement with theoretical and experimental results in the literature. The end effects are suppressed most when the gap between the sinker and the container wall is very narrow and the sinker is sufficiently long, in correspondence with the assumptions made in the semi-analytical derivations.

Finally, we have performed a numerical simulation of a cylinder falling in an infinitely extended tube with an incompressible piezoviscous fluid with reference parameters of concentrated sulphuric acid. The results were discussed regarding the value of pressure-viscosity β, finding a significant departure from the Newtonian behaviour at 10^{-5} Pa^{-1}. The numerical error of the results was heuristically estimated by comparing the solutions for two consecutive mesh refinement levels; real experimental parameters of the simulations could not be considered in detail due to the accuracy of the computations.

Bibliography

[1] Bridgman, P. W.: *The Effect of Pressure on the Viscosity of Forty-Three Pure Liquids.* Proc Am. Art. Acad. Sci. 1926, **61** (3), pp. 57-99.

[2] Průša, V.; Srinivasan, S.; Rajagopal, K. R.: *The role of pressure dependent viscosity in measurements with falling cylinder viscometer.* Int. J. Nonlin. Mech 2012,**47**(7), 743-750. DOI:10.1016/j.ijnonlinmec.2012.02.001

[3] Gurtin, M. E.. *An Introduction to Continuum Mechanics.* Academic Press, San Diego 1981. ISBN 0-12-309750-9

[4] Davis, L. A.; Gordon, R. B.: *Compression of Mercury at High Pressure.* J. Chem. Phys. 1967,**46**(7), pp. 2650-2660; DOI: 10.1063/1.1841095

[5] Barus, C.: *Isotherms, isopiestics and isometrics relative to viscosity.* Am J. Sci. 1893, **45**, pp. 87-96.

[6] Irving, J. B.; Barlow, A. J.: *An automatic high pressure viscometer.* J. Phys. E: Sci. Instrum. 1971, **4**, pp. 232-236.

[7] Harris, K. R.: *Temperature and Density Dependence of the Viscosity of Toluene.* J. Chem. Eng. Data 2000, **45**, pp. 893-897.

[8] Griest, E. M.; Webb, W.; Schiessler, R. W.:*Effect of Pressure on Viscosity of Higher Hydrocarbons and Their Mixtures.* J. Chem. Phys. 1958, **29**, pp. 711-720. DOI: 10.1063/1.1744579

[9] Harris, K. R.; Bair, S. *Temperature and Pressure Dependence of the Viscosity of Diisodecyl Phthalate at Temperatures between (0 and 100)°C and at Pressures to 1 GPa.* J. Chem. Eng. Data 2007, **52**, pp. 272-278.

[10] Jones, W.R., Jr. and Jansen, M.J. (2000), *Space Tribology*, Chapter 31 in *Modern Tribology Handbook* Vol 1, Editor, B. Bhusan, CRC Press LLC, Boca Raton, FI. DOI: 10.1201/9780849377877.ch31

[11] Hron, J.; Málek, J.; Nečas, J.; Rajagopal, K. R.: *Numerical simulations and global existence of solutions of two-dimensional flows of fluids with pressure- and shear-dependent viscosities.* Math. Comput. Simulation 2003, **61**, pp. 297-315.

[12] Hirn, A.; Lanzendörfer, M.; Stebel, J.:*Finite element approximation of flow of fluids with shear rate and pressure dependent viscosity.* IMA J. Numer. Anal. 2012 **32** (4), pp. 1604-1634. DOI:10.1093/imanum/drr033

[13] Gazzola, F.: *A note on the evolution Navier-Stokes equations with a pressure-dependent viscosity.* Z. angew. Math. Phys. 1997, **48**, pp. 760–773.

[14] Bulíček, M.; Málek, J.; Rajagopal, K. R.: *Mathematical analysis of unsteady flows of fluids with pressure, shear-rate, and temperature dependent material moduli that slip at solid boundaries.* SIAM J. Math. Anal. 2009, **41** (2), pp. 665–707.

[15] Viswanath, D. S., T. K. Ghosh, D. H. L. Prasad, N. V. K. Dutt, and K. Y. Rani: *Viscosity of liquids: Theory, estimation, experiment, and data.* Dordrecht: Springer 2007.

[16] Chan, R. K. Y.; Jackson, D. A.:*An automated falling-cylinder high pressure laser-Doppler viscometer.* J. Phys. E: Sci. Instrum. 1985, **18**, pp. 510-515.

[17] Liu, H.; Bau, H. H.; Hu, H. H.: *On the translation of a cylinder in a long tube.* Phys. Fluids (2004), **16** (4), pp. 998-1007.

[18] Schaschke, C.: High pressure viscosity measurement with falling body type viscometers. IReChe 2010,**2** (5). pp. 564-576. ISSN 2035-1755

[19] Lohrenz, J.; Swift, G.W.; Kurata, F. *An experimentally verified theoretical study of the falling cylinder viscometer.* AIChE J. 1960, **6** (4), pp. 547-550. DOI: 10.1002/aic.690060408

[20] Cristescu, N. D.; Conrad, B. P.; Tran-Son-Tay, R.: *A closed form solution for falling cylinder viscometers.* Int. J. Eng. Sci. 2002, **40** (6), 605–620.

[21] Hron, J.: *Fluid structure interaction with applications in biomechanics.* Doctoral thesis, Faculty of Mathematics and Physics, Charles University in Prague, 2001.

[22] Hron, J.; Málek, J.; Rajagopal, K. R.: *Simple flows of fluids with pressure-dependent visosities.* Proc. R. Soc. Lond. A 2001 **457**, 1603–1622.

[23] Lanzendörfer, M.: *Flows of incompressible fluids with pressure-dependent viscosity (and their application to modelling the flow in journal bearing).* Doctoral thesis, Faculty of Mathematics and Physics, Charles University in Prague, 2011.

[24] Boffi, D.; Gastaldi, L.: *On the quadrilateral $Q_2 - P_1$ element for the Stokes problem.* Int. J. Numer. Meth. Fluids 2002, **39**, pp. 1001–1011; DOI: 10.1002/d.358.

[25] Davis, T. A.: *Algorithm 832: UMFPACK, an unsymmetric-pattern multifrontal method.* ACM Transactions on Mathematical Software, vol 30, no. 2, June 2004, pp. 196-199. DOI: 10.1145/992200.992205

[26] Renardy, M.:*Parallel shear flows of fluids with a pressure-dependent viscosity.* J. Non-Newtonian Fluid Mech 2003,**114**, 229–236. DOI: 10.1016/S0377-0257(03)00154-X

[27] Denn, M.: *Pressure drop-flow rate equation for adiabatic capillary flow with a pressure- and temperature-dependent viscosity.* Polymer Eng. Sci. 1981, **21** (2) pp. 65-68.

[28] Suslov, S. A.; Tran, T. D.; *Revisiting plane Couette-Poiseuille flows of a piezo-viscous fluid.* Journal of Non-Newtonian Fluid Mechanics 2001, **154** (2-3). DOI: 10.1016/j.jnnfm.2008.04.010

[29] Rannacher, R.; Heywood, J. G.; Turek, S.: Artificial boundaries and flux and pressure conditions for the incompressible Navier-Stokes equations. Int. J. Numer. Meth. Fluids 1996, **22** (5), pp. 325-352. DOI: 10.1002/(SICI)1097-0363(19960315)22:5<325::AID-FLD307>3.0.CO;2-Y

[30] Kiran, E.; Sen, Y. L.: *High-pressure viscosity and density of n-alkanes.* Int. J. Thermophys. (1992) **13**, pp. 411–442.

[31] Zeng, M.; Schaschke, C.: *High pressure falling sinker liquid viscosity determination without supplementary density data: A new approach.* Int. J. Chem. Eng. (2009), vol. 2009. art. ID 747592, 8 pages. DOI:10.1155/2009/747592

[32] Park, N. A.; Irvine, T. F. Jr.: *Falling cylinder viscometer end correction factor.* Rev. Sci. Instrum. 1995, **66**(7), pp. 3982-3984; DOI: 10.1063/1.1145404

[33] Wehbeh, E. G.; Ui, T. J.; Hussey, R. G.: *End effects for the falling cylinder viscometer.* Phys. Fluids A 1993, **5**(1), pp. 25-33 ; DOI: 10.1063/1.858781

[34] Saad, Y.; Schultz, M. H.: *GMRES: A generalized minimal residual algorithm for solving nonsymmetric linear systems.* SIAM J. Sci. Stat. Comput. 1986, **7** (3), pp. 856-869.

[35] Li, X. S.: *An Overview of* SuperLU*: Algorithms, Implementation, and User Interface.* ACM Transactions on Mathematical Software 2005, **31** (3), pp. 302-325.

[36] Glowinski, R.; Pan, T.-W.; Hesla, T. I.; Joseph, D. D.; Periaux, J.:*A Fictitious Domain Method with Distributed Lagrange Multipliers for the Numerical Simulation of Particulate Flow.* Contemporary Mathematics 1998, **218**, pp. 121-137.

[37] Kondrat'ev, V. A.: *Asymptotic of solution of the Navier–Stokes equation near the angular point of the boundary.* J. Appl. Math. Mech. 1967, **31** (1), 125–129.

[38] Brdička, M.; Samek, L.; Sopko, B.: *Mechanika kontinua.* 2nd edition, Academia Praha 2000. ISBN 80-200-0772-5

[39] Fecko, M. *Diferenciálna geometria a Lieove grupy pre fyzikov.* Iris, Bratislava, 2004. ISBN 80-89018-10-6

A. Vector calculus

The next section serves only as a short reference of the vector analysis identities used. For a comprehensive coverage of the vector analysis, see [38] or one of the numerous textbooxs on fluid mechanics or electromagnetism. An introduction to differential geometry is given in [39].

A.1 Cylindrical coordinates

Physical quantities in space $\mathbb{R}^3$ may be expressed in cylindrical (polar) coordinates $[r, \varphi, z]$, related to the Cartesian coordinates $[x, y, z]$ as follows:

$$x = r\cos\varphi \tag{A.1a}$$
$$y = r\sin\varphi \tag{A.1b}$$
$$z = z \tag{A.1c}$$

The metric tensor takes the form

$$\mathbf{g}_{ij} = \begin{pmatrix} 1 & 0 & 0 \\ 0 & r^2 & 0 \\ 0 & 0 & 1 \end{pmatrix}.$$

The matrix of the metric tensor is diagonal as the coordinates are orthogonal.

A.1.1 Differential Operators

By $\mathbf{e}_i$ we will denote base physical vectors, $\mathbf{e}_i\mathbf{e}^i = 1$:

$$\mathbf{e}_i = g^{ij}\frac{\partial}{\partial x^j},$$

where the symbol $\frac{\partial}{\partial x^j}$ denotes covariant basis.

The nonzero Christoffel symbols are

$$\Gamma^r_{\varphi\varphi} = -r,$$

$$\Gamma^\varphi_{r\varphi} = \frac{1}{r}.$$

Introducing the covariant derivative

$$\nabla_j v^i = \frac{\partial v^i}{\partial x^j} + \Gamma^i_{jk}v^k,$$

we can write the differential operators in cylindric coordinates as follows:

Gradient of a scalar function

$$\nabla f = \frac{\partial f}{\partial r}\mathbf{e}_r + \frac{1}{r}\frac{\partial f}{\partial \varphi}\mathbf{e}_\varphi + \frac{\partial f}{\partial z}\mathbf{e}_z \tag{A.2}$$

Divergence of a vector field

$$\operatorname{div}\mathbf{v} \equiv \nabla\cdot\mathbf{v} = \frac{\partial v^r}{\partial r} + \frac{1}{r}v^r + \frac{1}{r}\frac{\partial v^\varphi}{\partial \varphi} + \frac{\partial v^z}{\partial z} = \frac{1}{r}\frac{\partial}{\partial r}\left(rv^r\right) + \frac{1}{r}\frac{\partial v^\varphi}{\partial \varphi} + \frac{\partial v^z}{\partial z} \tag{A.3}$$

The gradient of a vector field ($\mathbf{e}_{ij}$ is a shorthand for $\mathbf{e}_i \otimes \mathbf{e}_j$)

$$\begin{aligned}\nabla\mathbf{v} =& \frac{\partial v^r}{\partial r}\mathbf{e}_{rr} + \left(\frac{1}{r}\frac{\partial v^r}{\partial \varphi} - \frac{1}{r}v^\varphi\right)\mathbf{e}_{r\varphi} + \frac{\partial v^r}{\partial z}\mathbf{e}_{rz} \\ &+ \frac{\partial v^\varphi}{\partial r}\mathbf{e}_{\varphi r} + \left(\frac{1}{r}\frac{\partial v^\varphi}{\partial \varphi} + \frac{1}{r}v^r\right)\mathbf{e}_{\varphi\varphi} + \frac{\partial v^\varphi}{\partial z}\mathbf{e}_{\varphi z} \\ &+ \frac{\partial v^z}{\partial r}\mathbf{e}_{zr} + \frac{1}{r}\frac{\partial v^z}{\partial \varphi}\mathbf{e}_{z\varphi} + \frac{\partial v^z}{\partial z}\mathbf{e}_{zz}\end{aligned} \tag{A.4}$$

Convective derivative

$$(\mathbf{v}\cdot\nabla)\mathbf{v} = \left[v_r\frac{\partial}{\partial r} + \frac{v^\varphi}{r}\frac{\partial}{\partial \varphi} + v^z\frac{\partial}{\partial z}\right](v^r\mathbf{e}_r + v^\varphi\mathbf{e}_\varphi + v^z\mathbf{e}_z) =$$

$$\begin{aligned}&= \left[v^r\frac{\partial v^r}{\partial r} + \frac{v^\varphi}{r}\frac{\partial v^r}{\partial \varphi} - \frac{(v^\varphi)^2}{r} + v^z\frac{\partial v^r}{\partial z}\right]\mathbf{e}_r \\ &+ \left[v^r\frac{\partial v^\varphi}{\partial r} + \frac{v^\varphi}{r}\frac{\partial v^\varphi}{\partial \varphi} + \frac{v^\varphi v^r}{r} + v^z\frac{\partial v^\varphi}{\partial z}\right]\cdot\mathbf{e}_\varphi \\ &+ \left[v^r\frac{\partial v^z}{\partial r} + \frac{v^\varphi}{r}\frac{\partial v^z}{\partial \varphi} + v^z\frac{\partial v^z}{\partial z}\right]\mathbf{e}_z\end{aligned}$$

The Laplacian of is defined as the divergence of a gradient:

$$\Delta\mathbf{v} = \nabla\cdot(\nabla\mathbf{v}). \tag{A.5}$$

In the particular case of a vector field we get

$$\begin{aligned}\Delta\mathbf{v} = &\left[\tfrac{\partial^2 v^r}{\partial r^2} + \tfrac{1}{r}\tfrac{\partial v^r}{\partial r} - \tfrac{v^r}{r^2} - \tfrac{2}{r^2}\tfrac{\partial v^\varphi}{\partial \varphi} + \tfrac{1}{r^2}\tfrac{\partial^2 v^r}{\partial \varphi^2} + \tfrac{\partial^2 v^r}{\partial z^2}\right]\mathbf{e}_r \\ &\left[\tfrac{\partial^2 v^\varphi}{\partial r^2} + \tfrac{1}{r}\tfrac{\partial v^\varphi}{\partial r} - \tfrac{v^\varphi}{r^2} + \tfrac{2}{r^2}\tfrac{\partial v^r}{\partial \varphi} + \tfrac{1}{r^2}\tfrac{\partial^2 v^\varphi}{\partial \varphi^2} + \tfrac{\partial^2 v^\varphi}{\partial z^2}\right]\mathbf{e}_\varphi \\ &\left[\tfrac{\partial^2 v^z}{\partial r^2} + \tfrac{1}{r}\tfrac{\partial v^z}{\partial r} + \tfrac{1}{r^2}\tfrac{\partial^2 v^z}{\partial \varphi^2} + \tfrac{\partial^2 v^z}{\partial z^2}\right]\mathbf{e}_z\end{aligned}$$

Divergence of a tensor:

$$\begin{aligned}\nabla\cdot\mathbb{T} = &\left[\frac{\partial T^r_r}{\partial r} + \frac{1}{r}T^r_r + \frac{1}{r}\frac{\partial T^r_\varphi}{\partial \varphi} - \frac{1}{r}T^\varphi_\varphi + \frac{\partial T^r_z}{\partial z}\right]\mathbf{e}_r \\ &+ \left[\frac{\partial T^\varphi_r}{\partial r} + \frac{1}{r}\frac{\partial T^r_\varphi}{\partial \varphi} + \frac{1}{r}T^\varphi_r + \frac{\partial T^\varphi_z}{\partial z}\right]\mathbf{e}_\varphi \\ &+ \left[\frac{\partial T^z_r}{\partial r} + \frac{1}{r}\frac{\partial T^z_\varphi}{\partial \varphi} + \frac{1}{r}T^z_r + \frac{\partial T^z_z}{\partial z}\right]\mathbf{e}_z\end{aligned} \tag{A.6}$$

Previous formulae can be generalised for general tensorial fields using Leibniz rule with respect to tensor product $\mathbf{a}\otimes\mathbf{b}$.

A.1.2 Linear momentum balance in cylindric coordinates

Recall that constitutive relation reads

$$\mathbb{T} = -p\mathbb{I} + \mu(p)\left[\nabla\mathbf{v} + (\nabla\mathbf{v})^T\right].$$

Assuming circular symmetry

$$v^{\varphi} = 0, \quad \frac{\partial}{\partial \varphi} \equiv 0,$$

we can write the components of the symmetric velocity gradient in a compact form

$$\mathbb{D} = \begin{pmatrix} \frac{\partial v^r}{\partial r} & 0 & \frac{1}{2}\left(\frac{\partial v^r}{\partial z} + \frac{\partial v^z}{\partial r}\right) \\ 0 & \frac{v^r}{r} & 0 \\ \frac{1}{2}\left(\frac{\partial v^z}{\partial r} + \frac{\partial v^r}{\partial z}\right) & 0 & \frac{\partial v^z}{\partial z} \end{pmatrix}.$$

Taking the divergence of extra stress tensor $\mathbb{S} = 2\mu(p)\mathbb{D}(\mathbf{v})$, we find that

$$(\nabla \cdot \mathbb{S}) = \begin{pmatrix} 2\frac{\partial}{\partial r}\left(\mu(p)\frac{\partial v^r}{\partial r}\right) + \frac{2\mu(p)}{r}\frac{\partial v^r}{\partial r} - \frac{2\mu(p)v^r}{r^2} + \frac{\partial}{\partial z}\left[\mu(p)\left(\frac{\partial v^r}{\partial z} + \frac{\partial v^z}{\partial r}\right)\right] \\ 0 \\ \frac{\partial}{\partial r}\left[\mu(p)\left(\frac{\partial v^z}{\partial r} + \frac{\partial v^r}{\partial z}\right)\right] + 2\frac{\partial}{\partial z}\left(\mu(p)\frac{\partial v^z}{\partial z}\right) \end{pmatrix},$$

so there is no force in the $\mathbf{e}_{\varphi}$ direction. Summing up, we get the system

$$\frac{1}{r}\frac{\partial (r v^r)}{\partial r} + \frac{\partial v^z}{\partial z} = 0, \tag{A.7a}$$

$$\begin{aligned} \frac{\partial v^r}{\partial t} + v^r\frac{\partial v^r}{\partial r} + v^z\frac{\partial v^r}{\partial z} &= -\frac{\partial p}{\partial r} + 2\frac{\partial}{\partial r}\left(\mu(p)\frac{\partial v^r}{\partial r}\right) \\ &\quad + \frac{\partial}{\partial z}\left[\mu(p)\left(\frac{\partial v^r}{\partial z} + \frac{\partial v^z}{\partial r}\right)\right] + \frac{2\mu(p)}{r}\frac{\partial v^r}{\partial r} - \frac{2\mu(p)v^r}{r^2}, \end{aligned} \tag{A.7b}$$

$$\begin{aligned} \frac{\partial v^z}{\partial t} + v^r\frac{\partial v^z}{\partial r} + v^z\frac{\partial v^z}{\partial z} &= -\frac{\partial p}{\partial z} + \frac{\partial}{\partial r}\left[\mu(p)\left(\frac{\partial v^z}{\partial r} + \frac{\partial v^r}{\partial z}\right)\right] \\ &\quad + 2\frac{\partial}{\partial z}\left(\mu(p)\frac{\partial v^z}{\partial z}\right). \end{aligned} \tag{A.7c}$$

For the purpose of the finite element approximation, we will transform the last two equations in (A.7) to a formula with first derivatives only, in the same fashion as the weak formulation is derived. One option is to take the balance of mass and momentum

$$\frac{\partial \mathbf{v}}{\partial t} + (\mathbf{v} \cdot \nabla)\mathbf{v} = \nabla \cdot \mathbb{T},$$

multiply both sides by a smooth function $\mathbf{w}$, integrate over Ω and then use integration by parts:

$$\frac{\partial}{\partial t}\int_{\Omega} \mathbf{v} \cdot \mathbf{w}\ \mathrm{d}x + \int_{\Omega}[(\mathbf{v} \cdot \nabla)\mathbf{v}] \cdot \mathbf{w}\ \mathrm{d}x = -\int_{\Omega} \mathbb{T} : \nabla \mathbf{w}\ \mathrm{d}x + \int_{\Gamma_N} (\mathbb{T}\mathbf{n}) \cdot \mathbf{w}\ \mathrm{d}S.$$

The symbol ":" denotes Frobenius scalar product. Rewriting the above equation

in components using cylindrical coordinates, we obtain

$$\begin{aligned}
&\frac{\partial}{\partial t}\int v^r w^r r \ \mathrm{d}r \ \mathrm{d}z + \int \left(v^r \frac{\partial v^r}{\partial r} + v^z \frac{\partial v^r}{\partial z} \right) w^r r \ \mathrm{d}r \ \mathrm{d}z \\
&+\frac{\partial}{\partial t}\int v^z w^z r \ \mathrm{d}r \ \mathrm{d}z + \int \left(v^r \frac{\partial v^z}{\partial r} + v^z \frac{\partial v^z}{\partial z} \right) w^z r \ \mathrm{d}r \ \mathrm{d}z \\
&= \int 2\mu(p) \left[\frac{1}{r^2} v^r w^r + \frac{\partial v^r}{\partial r}\frac{\partial w^r}{\partial r} + \frac{1}{2}\left(\frac{\partial v^r}{\partial z} + \frac{\partial v^z}{\partial r} \right) \frac{\partial w^r}{\partial z} \right] r \ \mathrm{d}r \ \mathrm{d}z + \\
&\int 2\mu(p) \left[\frac{\partial v^z}{\partial z}\frac{\partial w^z}{\partial z} + \frac{1}{2}\left(\frac{\partial v^z}{\partial r} + \frac{\partial v^r}{\partial z} \right) \frac{\partial w^z}{\partial r} \right] r \ \mathrm{d}r \ \mathrm{d}z \\
&+ \int_{\Gamma_N} \mathbb{T}\mathbf{n} \cdot \mathbf{w} \ \mathrm{d}S.
\end{aligned} \tag{A.8}$$

The last term is treated as the Neumann-type boundary condition, so we did not expand the formula. Since w^r and w^z are independent (the identity has to hold for all smooth $\mathbf{w}$), terms pertaining to respective components of $\mathbf{w}$ can be separated, resulting in a system of two equations for unknown $v^r,\ v^z$.

The other option is to take classical formulation of momentum balance (A.7) and treat it as a system of three partial differential equations in *Cartesian* space spanned by variables $[r, z]$.

A similar procedure yields

$$\begin{aligned}
&\frac{\partial}{\partial t}\int v^r w^r \ \mathrm{d}r\mathrm{d}z + \int \left(v^r \frac{\partial v^r}{\partial r} + v^z \frac{\partial v^r}{\partial z} \right) w^r \ \mathrm{d}r\mathrm{d}z \\
&= -\int \left[p + 2\mu(p) \left(\frac{\partial v^r}{\partial r} + \frac{v^r}{r} \right) \right] \frac{\partial w^r}{\partial r} + \mu(p) \left(\frac{\partial v^r}{\partial z} + \frac{\partial v^z}{\partial r} \right) \frac{\partial w^r}{\partial z} \ \mathrm{d}r\mathrm{d}z \\
&+ \int \left(\frac{2\mu(p)}{r}\frac{\partial v^r}{\partial r} - \frac{2\mu(p)v^r}{r^2} \right) w^r \ \mathrm{d}r \ \mathrm{d}z \\
&+ \int_{\Gamma_N} T^{rr} n^r w^r + T^{zr} n^z w^r \ \mathrm{d}l,
\end{aligned} \tag{A.9a}$$

and, for the second equation,

$$\begin{aligned}
&\frac{\partial}{\partial t}\int v^z w^z \ \mathrm{d}r\mathrm{d}z + \int \left(v^r \frac{\partial v^z}{\partial r} + v^z \frac{\partial v^z}{\partial z} \right) w^z \ \mathrm{d}r\mathrm{d}z \\
&= \int \frac{\mu(p)}{r} \left(\frac{\partial v^z}{\partial r} + \frac{\partial v^r}{\partial z} \right) w^z \ \mathrm{d}r\mathrm{d}z \\
&- \int \mu(p) \left(\frac{\partial v^r}{\partial z} + \frac{\partial v^z}{\partial r} \right) \frac{\partial w^z}{\partial r} + 2\mu(p)\frac{\partial v^z}{\partial z}\frac{\partial w^z}{\partial z} \ \mathrm{d}r\mathrm{d}z \\
&+ \int_{\Gamma} T^{rz} n^r w^z + T^{zz} n^z w^z \ \mathrm{d}l.
\end{aligned} \tag{A.9b}$$

B. Contents of the attachment

A CD with supplementary data is attached to the thesis. The CD contains the source code of the finite element solver, auxiliary files for the computations (the meshes and input parameter files), data files with numerical results and the electronic version of the figures. See file `bender_pressure/readme.txt` for more information concerning the contents.

List of Figures

List of Tables

Nomenclature

Vector analysis		
p		scalar quantity
$\mathbf{v}$		vector quantity
$\mathbf{e}_i$		i-th basis vector
$\mathbb{T}$		tensorial quantity
∇p	$\frac{\partial p}{\partial x^i}\mathbf{e}_i$	gradient of a scalar
$\nabla \cdot \mathbf{v}$	$\mathrm{Tr}\,(\nabla \mathbf{v}) = \frac{\partial v^i}{\partial x^i}$	divergence of a vector field
$\mathbb{D}(\mathbf{v})$	$\frac{1}{2}[\nabla \mathbf{v} + (\nabla \mathbf{v})^T]$	
	$= \frac{1}{2}\left(\frac{\partial v^i}{\partial x^j} + \frac{\partial v_j}{\partial x_i}\right)\mathbf{e}_i \otimes \mathbf{e}^j$	symmetric part of velocity gradient
$\nabla \cdot \mathbb{T}$	$\frac{\partial T^{ij}}{\partial x^j}\mathbf{e}_i$	divergence of a tensor field
$\mathbf{v} \cdot \nabla \mathbf{v}$	$v^i \frac{\partial v^j}{\partial x^i}$	(the product part of) convective operator

Physical quantities			
symbol	unit	meaning	physical dimension
$\mathbf{r}$	[m]	position vector	
m	[kg]	mass	
t	[s]	time	
h	[m]	sinker length	
H	[m]	tube length	
R_1	[m]	sinker radius	
R_2	[m]	tube radius	
v^*	[m·s^{-1}]	FCV sinker velocity	
v^*_{term}	[m·s^{-1}]	theoretical value of terminal sinker velocity	
v^*_0	[m·s^{-1}]	numerical value of settling velocity	
a^*	[m·s^{-1}]	sinker acceleration	
g	[m·s^{-2}]	gravitational acceleratiom	
$\mathbf{v}$	[m·s^{-1}]	velocity	
p	[Pa]	pressure	[kg·m^{-1}·s^{-2}]
p_0		reference pressure for pressure-viscosity measurements	
p_{conf}		confining pressure in the FCV tube	
F	[N]	force	[kg·m·s^{-2}]
ρ_f	[kg·m^{-3}]	fluid density	
ρ_s		density of the FCV sinker	
μ	[Pa·s]	viscosity	[kg·m^{-1}·s^{-1}]
μ_0		reference viscosity	
β	[Pa^{-1}]	pressure-viscosity coefficient	
ECF	1	end correction factor	

Abbreviations

FCV	falling cylinder viscometer
NS,N.-S.	Navier-Stokes equations
	Navier-Stokes (Newtonian) fluid
FEM	finite element method
P-C	predictor-corrector method
2D	two-dimensional, planar
ECF	end correction factor
NGI	National Grid Infrastructure
CERIT	Centre for Education, Research and ICT innovations